OXFORD UNIVERSITY PRESS | Journal of Petrology

Draft Manuscript for Review

Links between calcite kimberlite, aillikite and carbonatite in West Greenland: Numeric modeling of compositional relationships

Journal:	*Journal of Petrology*
Manuscript ID	JPET-Feb-24-0032.R1
Manuscript Type:	Original Manuscript
Date Submitted by the Author:	n/a
Complete List of Authors:	Pilbeam, Llewellyn; University of Copenhagen Faculty of Science; Geological Survey of Denmark and Greenland Nielsen, Troels; Geological Survey of Denmark and Greenland, Mapping and Mineral Resources Waight, Tod; Department of Geosciences and Natural Resource Management, Geology Tappe, Sebastian; University of Tromso Faculty of Science, Geology
Keyword:	kimberlite, ultramafic, lamprophyre, magma, modelling
Journal of Petrology now offers Virtual Collections of published papers. You may choose up to three collections from the list below. Virtual collections will increase the visibility of your work.:	Ultramafic rocks < Material Themes, Continental Intraplate Magmatism < Province Themes, Partial Melting < Process Themes

Links between calcite kimberlite, aillikite and carbonatite in West Greenland: Numeric modeling of compositional relationships

PILBEAM L.H.[1,2], NIELSEN T.F.D.[2*], WAIGHT T.[1], TAPPE S.[3]

1. Department of Geosciences and Natural Resource Management (Geology Section), University of Copenhagen, Øster Voldgade 10, 1350 Copenhagen K, Denmark.
2. Geological Survey of Denmark and Greenland, Øster Voldgade 10, 1350 Copenhagen K, Denmark.
3. Department of Geosciences, UiT The Arctic University of Norway, Dramsveien 201, 9037 Tromsø, Norway.

*tfn@geus.dk

Submitted to Journal of Petrology 2024

Corresponding author: Troels F.D. Nielsen

ABSTRACT

Textural, mineralogical and mineral compositional observations in a suite of Neoproterozoic aillikite and calcite kimberlite dykes from southern West Greenland point to consistent variations in melt major element compositions among these silica-undersaturated magma types, with notably higher bulk SiO_2/CO_2, H_2O/CO_2 and K_2O for aillikite compared to calcite kimberlite. Bulk rock arrays, together with field and petrographic observations, emphasize that flow sorting of olivine and other crystalline phases during magma emplacement is important in controlling the compositions of individual samples from these ultramafic dykes. Flow sorting together with petrographic evidence for variable overall proportions of entrained lithospheric mantle material result in scatter on element–element plots, which makes the interpretation of regional scale major and trace element geochemical datasets difficult. We argue that a significant proportion of the regional Ni—MgO variation in the ultramafic dyke suite of SW Greenland is due to variation in the proportion of an entrained refractory lithospheric mantle component. Therefore, ratios of elements to MgO can be used as proxies for melt compositions. Ratios of SiO_2, TiO_2, Al_2O_3, FeO and K_2O over MgO are systematically higher, and CO_2/MgO lower, in aillikites compared to calcite kimberlites. The trace element patterns of the calcite kimberlite and aillikite dykes show strong similarities in incompatible element concentrations, resulting in overlapping ratios for the highly to moderately incompatible elements. However, differences in Zr-Hf concentrations between rock types imply differences in mantle source mineralogy. Guided by our observations, we present mixing models that demonstrate that partial flux-melting of phlogopite–ilmenite metasomes within the cratonic mantle lithosphere, initiated by infiltrating asthenosphere-derived carbonatitic melts previously identified to represent parental liquids to calcite kimberlite, is capable to produce the geochemical characteristics of the aillikites and mela-aillikites in West Greenland.

KEYWORDS

Kimberlite, aillikite, carbonatite, modeling, flux-melting, glimmerite, mineral chemistry, geochemistry

INTRODUCTION

Kimberlites and related rocks form from volatile-rich ultramafic magmas generated in the lower reaches of thick continental lithosphere or below – typically within the diamond stability field in excess of 150 km depth (e.g., Dawson, 1971; le Roex, 1986; Mitchell, 2008; Tappe *et al.*, 2018; Giuliani *et al.*, 2020). Kimberlitic-affinity rocks comprise occurrences of kimberlite *sensu stricto* such as archetypal kimberlites in southern Africa (Mitchell, 1986), as well as more potassic ultramafic rock types such as orangeites (Mitchell, 1995) and ultramafic lamprophyres (UMLs) including the carbonate-rich variety aillikite (Tappe *et al.*, 2005). Links between these magma types, carbonatites and amphibole-phenocrystic ULMs almost certainly exist, but are not straightforward to decipher (e.g., Foley *et al.*, 2009; Tappe *et al.*, 2011a, 2017a; Smith *et al.*, 2013; Rooney *et al.*, 2020; Sarkar *et al*., 2023, Wang et al., 2021). Further complication arises from the fact that even kimberlites (*sensu strictu;* Tappe et al., 2005) show considerable variability in their major element compositions, both at the scale of individual volcanic fields and entire cratons, as well as globally (e.g., Kjarsgaard *et al*., 2009; Pearson *et al.*, 2019).

Kimberlitic-affinity rocks are characterized by extreme enrichment in very incompatible trace elements (VICEs, Pilbeam *et al.*, 2023), e.g., 100-500 times upper mantle values of LREE, Ba, U, Th, Nb, Ta, but only a modest enrichment in moderately incompatible trace elements (MICEs, Pilbeam *et al.*, 2023), e.g., ~1-10 times upper mantle values of HREE and Zr-Hf. This characteristic incompatible trace element pattern requires low degree partial melting of a garnet-bearing peridotitic mantle source (e.g., Ringwood *et al*., 1992; Tainton & McKenzie, 1994; Becker & le Roex., 2006; Pilbeam *et al*., 2013), in the presence of CO_2-H_2O volatile components (Foley *et al.*, 2009; Tappe *et al.*, 2017a).

Kimberlitic-affinity rocks are very heterogeneous with a high proportion of entrained mantle material. In order to study the melt components in kimberlitic occurrences it is necessary to assess the relative contributions of the melt and the various entrained and

partially assimilated mantle-derived xenocrysts and micro-xenoliths to the bulk composition. Some bulk concentrations of trace elements are very high in kimberlitic magmas compared to other mantle-derived magmas, e.g., ~1000 μg/g Ni in kimberlite versus ~200 μg/g Ni in MORB (Arevalo & McDonough, 2010). Such elements are buffered with respect to melt fraction in both the melt and the residue during partial melting due to their compatibility in olivine. They are too high in kimberlitic-affinity magmas to represent melts derived from peridotitic mantle sources by anything other than extremely high degrees of partial melting, a suggestion discounted by the high concentrations of incompatible trace elements and volatiles (Arndt, 2003; Tappe *et al.*, 2018). Most kimberlitic-affinity magmas are therefore to some degree contaminated by lithospheric mantle materials (Fraser & Hawkesworth, 1992; Pearson *et al.*, 2019).

A series of textural and mineral compositional studies corroborates this geochemical observation, showing that a significant proportion of 'kimberlitic' olivine is derived from disaggregated peridotite xenoliths (Nielsen & Sand, 2008; Kamenetsky *et al*., 2008; Brett *et al.*, 2009; Arndt *et al*., 2010, 2022; Pilbeam *et al.*, 2013, 2023; Giuliani, 2018; Shaikh *et al.*, 2021). A further proportion of the olivine in kimberlites is most easily reconciled with having grown in response to of resorbtion of orthopyroxene (Russell *et al.*, 2012,) also referred to as DFC (digestion fractional crystallization, Pilbeam *et al*., 2013).

The classification of this varied group of volatile-rich ultramafic rocks is based on the compositions of the liquidus parageneses and the groundmass phases that clearly have crystallized from melt components (Mitchell, 1995; Nielsen & Jensen, 2005; Tappe *et al.*, 2005). For example, aillikites and orangeites contain phlogopite with Fe^{3+} substitution and zonation toward tetraferriphlogopite rather than low Fe^{T} and Al^{3+} and Ba enrichment seen in kimberlites (Mitchell, 1995; Tappe et al., 2005). Furthermore, liquidus clinopyroxene and increased modal phlogopite are present in aillikites as well as mela-aillikites (Tappe et al., 2005). but not in kimberlites Kimberlites also have different groundmass spinel

compositions compared to those characteristic for aillikites and orangeites (Mitchell, 1995). These differences in liquidus mineralogy, including mineral compositions, reflect differences in parental melt compositions. However, the heterogeneous nature of kimberlitic-affinity rocks typically masks the differences in bulk rock major and minor element compositions.

Here we study the petrogenetic relationship between a suite of Neoproterozoic ultramafic lamprophyre dykes (aillikites and mela-aillikites) and the Majuagaa calcite kimberlite dyke in southern West Greenland (Larsen & Rex, 1992; Mitchell *et al*., 1999; Nielsen *et al.*, 2009). The aim is to identify, describe and quantitatively model the proportions of the components that sum up to the bulk compositions of four representative kimberlite and aillikite occurrences in West Greenland, a region known for its abundance of well-preserved kimberlites and related rocks including intrusive carbonatites. Our study builds on and complements the isotopic work by Tappe et al. (2011a), but uses a different approach, namely focusing on petrographic observations and major–minor element compositions of rocks and minerals. In addition to the established differences in petrography, liquidus mineralogy and phlogopite compositions (Nielsen *et al.*, 2009), we describe the systematic compositional variations in olivine and apatite in the fresh kimberlite, aillikite and mela-aillikite dykes. We demonstrate that, by using bulk rock plots of elements relative to MgO contents, the effect of variable olivine contents can be largely negated so that more systematic relationships between melt components can be recognized from the geochemical data. The identified differences are used to construct a major and minor element mixing model that explores the petrogenetic links between calcite kimberlite, aillikite, mela-aillikite and carbonatite components of the deep-sourced volatile-rich ultramafic magmatism in West Greenland, with relevance to similar associations worldwide.

GEOLOGICAL SETTING

Samples used in this study originate from three aillikite localities and one kimberlite occurrence across the boundary between the ca. 1.8 Ga Nagssugtoqidian mobile belt (re-worked Archean) (Connelly *et al.*, 2006) and the ca. 3.0-2.7 Ga North Atlantic Craton of southern West Greenland (e.g., Nutman *et al*., 2004; Windley & Garde, 2009; McIntyre *et al*., 2021). The nature of the underlying mantle is constrained by rhenium-depletion and Pb-Pb model ages (2.7-3.2 Ga) for mantle peridotite and eclogite xenoliths from West Greenland that are in good agreement with North Atlantic Craton formation models developed mainly on the basis of crustal bedrock geology (Wittig *et al.*, 2008; Wittig *et al*., 2010; Tappe *et al.*, 2011b). Potassic metasomatic overprinting of the wider North Atlantic Craton lithospheric mantle is evident from phlogopite-rich peridotite and glimmerite xenoliths, rare in kimberlite but more common in aillikite and mela-aillikite occurrences (e.g., Garrit, 2000; Larsen & Garrit, 2005; Tappe *et al.*, 2006; Aulbach *et al.*, 2017a). The timing of these metasomatic events is poorly constrained but has been related to the 1.2 Ga lamproitic dyke swarms in the Sisimiut region (Nielsen *et al.*, 2009; Secher *et al.*, 2009), as well as to collisional events during Laurentia assembly at ca. 2.1-1.8 Ga (Aulbach *et al*., 2019).

FIELD DESCRIPTIONS AND SAMPLE SELECTION

Samples were chosen to be representative of and span the range in volatile-rich ultramafic magma types found within the study area in southern West Greenland (Nielsen *et al.*, 2009, Fig. 1). The ca. 558 Ma old Majuagaa dyke in the Maniitsoq region on the Archean craton (Tappe *et al.*, 2011a) is an exceptionally fresh and well-characterized CO_2-rich calcite kimberlite (Nielsen *et al*., 2006; Nielsen & Sand, 2008; Pilbeam *et al*., 2013, 2023). A hundred kilometers north towards the Nagssugtoqidian mobile belt in the Sarfartoq region, the ca. 582 Ma P-Dyke and the Sarfartuup Nuna South dyke (Secher *et al.*, 2009) were sampled in the Archean foreland to the mobile belt. The P-Dyke is transitional between

kimberlite and aillikite, and the Sarfartuup Nuna South dyke is an aillikite (Nielsen *et al.*, 2009). The ca. 587 Ma Maniitsorsuaq dyke in the Sisimiut region (Scott, 1981), located a farther 100 km to the northwest within a Paleoproterozoic terrane and at some distance to the exposed Archean craton, had previously been classified as an aillikite based on its mineralogy (Nielsen *et al.,* 2009). This dyke is re-classified here as a mela-aillikite based on more detailed groundmass petrography and mineral compositions.

In general, the kimberlitic-affinity rocks of southern West Greenland occur as dykes, sheets, blows and sills (Larsen & Rex, 1992). The surface expressions of dykes may be followed for several kilometers as multiple en-echelon segments that bifurcate and anastomose. Minor carbonate-enriched sills are associated with larger aillikite dykes. Evidence for physical sorting of solid phases during magma flow is apparent from the concentration of mantle-derived xenoliths within the central portions of dykes (Fig. 2a), whereas outer parts near dyke margins show lateral and laminar flow parallel to the contacts. Flow sorting is evident mainly by the distribution of olivine megacrysts and transported fragments of the subcontinental lithospheric mantle (SCLM) (Fig.2b-d). Carbonate segregation lenses may represent *in-situ* pockets of evolved melt. Carbonate-rich veins occur in the vicinity of dyke margins. They cross-cut the flow-induced fabric. They are interpreted as late-stage evolved melts/fluids that were injected back into the partly solidified dykes (back-veining). Alteration of the host basement gneisses is minor, although Scott (1977) reports pink discoloration along the dyke contacts in the Sisimiut region.

Field observations, petrography and geochemistry of the Majuagaa calcite kimberlite dyke (Fig. 1) are reported and discussed in detail in Jensen *et al.* (2004), Nielsen & Jensen (2005), Nielsen & Sand (2008) and Pilbeam *et al*. (2013, 2023). No new fieldwork was carried out at Majuagaa during this current study. Figure 2d shows lateral and laminar flow in an upturned boulder of Majuagaa kimberlite.

The Sarfartuup Nuna South aillikite in the Sarfartoq region (Fig. 1) is a ENE striking

dyke exposed over a length of >2 km. At two en-echelon dyke segments are observed with one site exhibiting dyke bifurcation. The Jesper blow is associated with the Sarfartuup Nuna South dyke. Magmatic flow alignment was observed in larger aillikite boulders of the distinct train of boulders along the inferred dyke trend. Mantle-derived xenoliths and megacrysts are relatively rare in this aillikite dyke, but harzburgite, dunite and glimmerite xenoliths were identified. Four new samples (51353x) were collected for this study to complement seven samples (4919xx) collected during previous fieldwork (Jensen *et al*., 2004).

The P-Dyke in the Sarfartoq region (Fig. 1) is ~1 km long and approximately East-West trending, sub-parallel to the host basement gneiss foliation. In the field, the P-Dyke is suggested to be ~3 m thick in the east and <0.5 m wide in the west. The only *in-situ* outcrop is heavily weathered. A total of twelve samples was collected along the length of the dyke (513501-513512), but only a single sample proved to have low serpentine content. Dunite, garnet harzburgite and lherzolite xenoliths, 2 to 20 cm in diameter, occur, whereas glimmerite xenoliths appear to be absent.

The Maniitsorsuaq mela-aillikite dyke in the Sisimiut region consists of a sub-vertical NW-SE trending system of en-echelon segments and bifurcating branches along the southern coast of Maniitsorsuaq Island (Fig. 1). One dyke segment can be followed for >800 m along strike. Another segment extends inland with outcrops exposing a 75 m vertical section in the dyke. Where thicker, magmatic foliation is well developed parallel to the dyke margins (Fig. 2a) and interpreted as flow-related, with xenoliths concentrated towards the dyke center (Fig. 2b). Flow structures are also developed around mantle-derived xenoliths (Fig. 2b), and differential weathering typically creates variations in relief at dyke surfaces (Fig. 2b). For this volatile-rich ultramafic dyke occurrence, the previously suggested distinction between xenolith-rich and xenolith-poor segments could not be confirmed during our fieldwork (cf., Scott, 1977). We only identified flow sorting of xenoliths and megacrysts towards the dyke

center, as well as magmatic foliation along the dyke margins and variable degrees of serpentinization. The xenolith assemblage at Maniitsorsuaq comprises abundant dunites and harzburgites and rarer garnet lherzolites plus minor glimmerite (phlogopite and phlogopite-ilmenite intergrowth). Ilmenite megacrysts also occur. All types of xenoliths range in size between 2 and 20 cm. Twelve samples from the Maniitsorsuaq dyke system (51355x-51359x; and 5179xx) represent the observed branches and textural variations (Fig. 2c). Of these samples, ten have low serpentine content and two are highly serpentinized (513567 and 513595).

PETROGRAPHIC OBSERVATIONS

Majuagaa calcite kimberlite

The petrography of the Majuagaa calcite kimberlite and the implications for parental kimberlite liquids have been discussed extensively (Nielsen & Jensen, 2005; Nielsen & Sand, 2008; Pilbeam *et al*., 2013; 2023). The macrocryst and megacryst assemblage comprises olivine (40-60 vol.% of the bulk rock), ilmenite (~5 vol.%), garnet (~1 vol.%) and minor heavily reacted orthopyroxene and clinopyroxene. The kimberlite groundmass consists of olivine microcrysts with cores that are probably of xenocrystic origin (Pilbeam *et al.,* 2013), anhedral olivine fragments and euhedral ilmenite/geikielite, ulvöspinel, Ba-rich phlogopite and apatite crystals set in an interstitial mesostasis of calcite, dolomite and locally apatite. Perovskite occurs as a reaction product after ilmenite/geikielite, but also as rare atoll-textured and oscillatory-zoned groundmass crystals. Very minor serpentine occurs along some olivine grain margins and also in the groundmass as a local replacement product after calcite and dolomite. A suite of rare accessory phases has been identified by EDS (energy dispersive spectroscopy) and includes sulphides, sulphates, baddeleyite, strontianite and REE-carbonates.

Several new observations are pertinent to this study. Two distinct textural types of

apatite are present at Majuagaa. Type 1 apatite occurs as euhedral prisms (5-10 μm length) throughout the groundmass (Fig. 3a), whereas Type 2 apatite forms irregular poikilitic patches up to 100 μm across and mainly associated with carbonate-rich segregations in the kimberlite groundmass. Type 2 apatite enclose Type 1 apatite and infill between matrix calcite and is one of the last phases to have crystallized (Fig. 3a). Calcite, especially in samples low in olivine, is commonly present as poikilitic (optically continuous) groundmass domains that enclose all other phases except for dolomite and Type 2 apatite. In the Majuagaa kimberlite, calcite is also present as microphenocrysts (Fig. 3b). Dolomite is interstitial to larger groundmass calcite domains and contains inclusions of all other phases. Calcite and dolomite show extensive blebby exsolution from each other implying a magmatic origin.

P-Dyke (transitional kimberlite–aillikite)

Most samples from the P-Dyke are heavily serpentinized compared to those from the other volatile-rich ultramafic dyke occurrences in West Greenland, and only sample 513512 is unaltered. It is composed of rounded olivine macrocrysts (50-60 vol.%), fragmented phlogopite plates, euhedral spinel and perovskite groundmass crystals, plus apatite prisms set in a mesostasis of calcite and dolomite. Clinopyroxene is not observed in the groundmass. Serpentine occurs both as pseudomorphs of olivine macrocrysts and as pervasive replacement of groundmass carbonates. Groundmass perovskite, phlogopite, apatite and spinel are unaffected by the serpentinization.

Maniitsorsuaq type mela-aillikites

Consistent with descriptions of aillikites and mela-aillikites from Labrador (Tappe *et al.*, 2004, 2006, 2008), the Maniitsorsuaq occurrence in West Greenland is best described as a mela-aillikite. The amount of primary groundmass clinopyroxene exceeds that of modal

carbonates (see Tappe *et al*., 2005). The Maniitsorsuaq mela-aillikite dyke consists of complexly-zoned olivine macrocrysts and megacrysts (20-30 vol.%) set in a groundmass (Fig. 3c) of phlogopite (~30 vol.%) and clinopyroxene (~30 vol.%), as well as euhedral spinel, perovskite and apatite, with minor late-stage magmatic carbonate (~5 vol.%). Serpentine is an alteration product along olivine rims and in some samples it pervasively replaces other groundmass minerals (Fig. 3d). Olivine macrocrysts (both normally and reversely zoned) reveal more complex compositional zoning than observed for olivine in the Majuagaa calcite kimberlite dyke (Pilbeam *et al*., 2013). Euhedral, zoned spinel up to 100 μm in diameter is abundant in the groundmass. Very minor euhedral ilmenite is present in groundmass carbonate domains and as inclusions in margins of olivine macrocrysts. Euhedral groundmass perovskite up to 100 μm in diameter is common and also occurs as inclusions in all other phases except for olivine.

Clinopyroxene forms elongate zoned microphenocrysts up to 150 μm in length typically enclosed in phlogopite, apatite and carbonate. The clinopyroxene microphenocrysts may host small olivine inclusions and compositional zoning is either reverse with increasing Mg# from core to margin, or irregular. Phlogopite flakes and plates (50-500 μm) exhibit complex zoning. The margins of phlogopite plates enclose groundmass spinel, perovskite, clinopyroxene and apatite, and in some cases fill interstitial space between olivine macrocrysts. Phlogopite cores may show reaction textures and be resorbed. They probably have an antecrystic or xenocrystic origin (Fig. 3e) (e.g., Giuliani *et al.*, 2016). Rare macrocrysts, megacrysts and xenoliths of ilmenite (up to 5 cm in diameter), with extensive spinel reaction rims, are present (Fig. 3f). EDS investigations confirm the presence of baddeleyite and barite in the groundmass. The phlogopite plates of entrained glimmerite xenoliths are commonly fractured and cores may show resorption (Fig. 3g).

Sr- and REE-carbonates appear to be absent in the Maniitsorsuaq mela-aillikite. Euhedral prismatic apatite crystals up to 100 μm in length may be enclosed in groundmass

phlogopite and carbonate. Apatite may also occupy interstitial spaces between olivine macrocrysts and microphenocrysts of spinel, perovskite, clinopyroxene and phlogopite. Clusters of apatite needles may form acicular sprays into groundmass carbonate domains. Calcite and very minor dolomite (<1 vol.%) enclose apatite, clinopyroxene, phlogopite, Fe-Ti-oxides and olivine, and the carbonates typically fill interstitial space within the groundmass.

Modal and textural variability is observed for the Maniitsorsuaq mela-aillikite dykes. The flow-banding in samples from closer to the dyke margins is defined by variable proportions of entrained olivine and SCLM fragments (e.g., 517905). Near margins, clinopyroxene and phlogopite are more abundant, and they have smaller crystal sizes compared to the dyke interiors. In dyke margin samples, clinopyroxene forms 5-20 μm long prismatic crystals that appear as high-birefringence masses in cross-polarized light. The phlogopite plates in these samples are 50-100 μm in size, slightly larger than the clinopyroxene crystals. In contrast, the more massive textured central portions of the Maniitsorsuaq mela-aillikite dykes (e.g., 517910) contain higher abundances of olivine macrocrysts and groundmass carbonate. Moreover, the clinopyroxene and phlogopite crystals are larger (up to 150 and 500 μm, respectively) compared to their analogs at the dyke margins. Although clinopyroxene and phlogopite are modally dominant in the dyke interiors, a decrease in abundance relative to the dyke margins is noted.

In general, the groundmass varies at Maniitsorsuaq from calcite-rich to serpentine-rich. Contacts between serpentine and calcite may be sharp or diffuse. Even the most calcite-rich groundmass domains exhibit minor replacement by serpentine, and the most serpentinized domains preserve remnants of calcite.

The aillikite at Sarfartuup Nuna South is comparable to the Maniitsorsuaq mela-aillikite in most respects, except for a lower clinopyroxene content (<5 vol.%) and a groundmass that is richer in carbonates (10-20 vol.%). Some samples are rich in olivine

macrocrysts, whereas others have a higher proportion of clinopyroxene, phlogopite and calcite, which is likely a consequence of flow sorting during magma emplacement. The extent of serpentinization of groundmass phases and olivine grains is variable.

Summary of petrographic observations and order of crystallization

The petrographic observations made for the Majuagaa calcite kimberlite (Nielsen & Sand, 2008; Nielsen *et al.,* 2009; Pilbeam *et al.,* 2013, 2023) and the Sarfartuup Nuna South and Maniitsorsuaq aillikite and mela-aillikite dykes (this study) are summarized here and in Figure 4. Notable petrographic differences between the calcite kimberlite and the aillikite/mela-aillikite parageneses (Fig. 4) are the absence of groundmass clinopyroxene and brown phlogopite in the calcite kimberlite dyke, which is uniquely characterized by abundant Mg-rich ilmenite and geikielite, rare perovskite, late-stage phlogopite zoned toward kinoshitalite rims (i.e., Ba-rich), and abundant groundmass carbonates (Nielsen *et al.,* 2009). In contrast, the aillikites contain groundmass clinopyroxene, brown phlogopite zoned toward tetraferriphlogopite rims, abundant early-stage perovskite, and relatively small amounts of groundmass carbonates. The P-Dyke is transitional between the Majuagaa calcite kimberlite and the aillikites/mela-aillikites because it lacks groundmass clinopyroxene but contains brown phlogopite with Al- and Ba-poor but Fe-rich rims.

ANALYTICAL METHODS

Detailed analytical protocols and descriptions of used methods are found in SI1. In addition to the new data reported, the published major and trace element compositions of the Majuagaa calcite kimberlite (Nielsen & Sand, 2008) and the Sarfartuup Nuna South aillikite (Nielsen *et al.*, 2009) are also used in this paper. For all samples discussed in this paper, an internally consistent set of total carbon concentrations (CO_2) was determined by the LECO method at ACME labs in Canada.

MINERAL CHEMISTRY: RESULTS AND IMPLICATIONS

Within the main body of this paper, we report representative mineralogical data pertinent for our subsequent modeling of the magmatic evolution of calcite kimberlites, aillikites and mela-aillikites in West Greenland. Where appropriate, we also include first interpretations of the mineral chemistry data, with implications for magma petrogenesis, which then lead directly to the presentation of bulk rock geochemistry results for our samples. Tables present representative sets of analyses. The full data sets are found in the supplementary information (S2-4 and SI5-SI9), and also at https://doi.org/10.22008/FK2/6DVABJ.

Olivine

Adding to the existing data for the Majuagaa calcite kimberlite (Nielsen & Sand, 2008), we report 1450 new olivine analyses by EPMA from six samples of the Sarfartuup Nuna South aillikite and 110 new analyses from three samples of the Maniitsorsuaq mela-aillikite (SI2). Most olivine analyses represent core-to-rim transects. We determined compositions for grains that would be petrographically defined as: macrocrysts/phenocrysts (e.g., Mitchell, 2008); Type I and II (Kamenetsky *et al.*, 2008; Brett *et al.*, 2009), and we also include 'tabular' grains (Arndt *et al*., 2010; Shaikh *et al.*, 2021). However, as in the Majuagaa calcite kimberlite (Pilbeam *et al*., 2013), we observe a continuity between smaller grains with higher margin/core ratios and subhedral to euhedral shapes, and larger grains with lower margin/core ratios leading to more rounded shapes. The dataset for the Sarfartuup Nuna South aillikite is representative of the olivine zoning types present at this occurrence, but not of their relative proportions. The reconnaissance olivine dataset for the Maniitsorsuaq mela-aillikite is supplementary to the Sarfartuup Nuna South data. It comprises only four analyses of larger rounded normally zoned grains without transects across the reversely zoned grains. The data are shown in Figs 5 and 6.

394 The compositions of cores of the zoned olivine grains from the Sarfartuup Nunat
395 South aillikite form diffuse clusters in Ni vs. Fo space (Fig. 5a) and vary between 750±250
396 μg/g Ni at ~Fo80 and 3000±500 μg/g Ni at ~Fo92. One olivine core has ~750 μg/g Ni at
397 ~Fo75. The Maniitsorsuaq mela-aillikite olivine cores (Fig. 5b) have a lower range in Fo and
398 Ni: ~1300 μg/g Ni at ~Fo80 to 2500±500 μg/g Ni at ~Fo90. It must be kept in mind,
399 however, that this dataset is limited to 110 analyses. The olivine cores in both dykes have
400 <2000 μg/g Ca. Small homogeneous groundmass olivine grains with no apparent core-
401 margin zonation occur in the Sarfartuup Nuna South aillikite and such grains have been
402 considered as microphenocrysts in other kimberlite and aillikite occurrences worldwide
403 (e.g., Kamenetsky *et al.*, 2008; Tappe *et al.*, 2009; Giuliani, 2018). These grains show the
404 same compositional range in Fo, Ni, Ca and Mn as the much larger zoned olivine
405 macrocrysts (Fig. 5c).
406 Figures 6 a-d shows transects across two normally and two reversely zoned olivine
407 crystals from the Sarfartuup Nunat South aillikite (Table SI2). The reversely zoned grains
408 contain an additional zone between core and margin in which Ni and Fo increase up to a
409 maximum of 3000 μg/g Ni at Fo86 to Fo89. Ca and Mn increase from below detection limit
410 in the cores to maximum values of 7000 μg/g and 4000 μg/g, respectively, at the grain edges
411 (SI2).
412 The two examples of olivine grains from Maniitsorsuaq mela-aillikite (Figs. 6e-f) have
413 complexly zoned cores surrounded by zones with decreases in Ni to ~1000 μg/g at ~Fo84, and
414 a marked rim with decrease in Ni and increases in Fo and CaO (Table SI2). Moving outwards
415 from the core of Maniitsorsuaq mela-aillikite olivines (Fis. 6e-f), Ni first decreases at near
416 constant forsterite content from ~2500 μg/g Ni and ~Fo88 to ~1500 μg/g Ni and ~Fo88.4 and
417 back up to ~2500 ppm Ni. This is followed by a region where Ni decreases to 1500-1000 μg/g
418 and ~Fo84. An up to 15 μm wide outer rim has grown on many grains with Ni decreasing

419 towards 500 μg/g at increasing MgO and reaching Fo87.

420

421 ***Implications of the olivine data***

422

423 Olivine cores

424

425 The cores of the olivine grains in the aillikites and mela-aillikites partially overlap with the
426 field of olivine compositions from peridotitic mantle xenoliths in southern West Greenland
427 (Figs 5). Such a relationship is also observed for the Majuagaa calcite kimberlite (Nielsen &
428 Jensen, 2005; Nielsen & Sand, 2008) and many other well-studied kimberlite provinces
429 worldwide (e.g., Brett *et al.*, 2009; Bussweiler *et al*., 2015; Giuliani, 2018; Shaikh *et al.*,
430 2021; Abersteiner *et al.*, 2022). In line with these investigations and the same petrographic
431 and compositional arguments, we interpret the cores of the olivine grains in aillikites and
432 mela-aillikites from West Greenland to be of xenocrystic origin. The olivine core
433 compositions at lower Ni and Fo contents are interpreted to indicate that a greater proportion
434 of olivine in aillikites/mela-aillikites is derived from disaggregated metasomatized and fertile
435 peridotite xenoliths, compared to the more refractory olivine xenocrysts in the Majuagaa
436 calcite kimberlite.

437 Homogenous groundmass olivine

438

439 The compositions of the unzoned olivine grains in the groundmass of Sarfartuup Nuna South
440 aillikite overlap with those of the cores and margins of the zoned olivine grains in the same
441 samples (Fig. 5c). This wide compositional range is difficult to reconcile with a phenocrystic
442 cognate origin for these homogeneous grains. The compositions are consistent with the
443 groundmass olivine grains representing originally zoned crystals that had cognate olivine
444 margins. Such grains were subsequently disaggregated and broken into small and more
445 homogenous fragments during magma ascent. The observation of rare, zoned olivine
446 fragments, some of which with incomplete margins, supports this interpretation. The

implication is that all magmatic olivine crystallization in the Sarfartuup Nuna South aillikite occurred as homogeneous nucleation and overgrowth on olivine xenocrysts. Furthermore, this suggests that olivine crystallization in the aillikite magma started at upper mantle levels prior to entering the crust, and it facilitated flow-induced fracturing of already zoned olivine crystals (e.g., Moore *et al.*, 2020; Shaikh *et al.*, 2021).

Crystallization conditions as recorded by olivine margins

In general, olivine in the aillikite dykes studied here exhibits more complex zoning patterns than observed in the Majuagaa calcite kimberlite (Nielsen & Sand, 2008; Pilbeam *et al*, 2013), with xenocrystic cores representing a smaller proportion of each crystal investigated. The complex zoning patterns for olivine in the Greenland aillikites and mela-aillikites are consistent with Tappe *et al*. (2006), who observed mostly complexly grown magmatic olivine in aillikites from Aillik Bay in Labrador, very different from olivine in kimberlites (Arndt *et al.,* 2010; Giuliani, 2018; Abersteiner *et al.,* 2022).

The inner margins of the reversely zoned olivine crystals in the aillikite and mela-aillikite dykes show increasing Ni of up to 2000-3000 μg/g and increasing Fo of up to 86-90 (Figs 5e-f). In contrast, the inner margins of olivines in the Majuagaa calcite kimberlite are characterized by Fo contents that do not exceed the value for the margin with near constant Fo and decreasing Ni. The compositions of these inner margins can be reproduced by diffusion of Mg and Fe between olivine cores and crystal margins (Pilbeam *et al*., 2013). The inner olivine margins of normally zoned crystals in the Sarfartuup Nuna South aillikite show decreasing Fo and Ni. We relate such zoning to fractional crystallization rather than to diffusional equilibration between cores and margins. The implication is that the olivine margins in the aillikite dykes are truly cognate. The olivine rims crystallized from the aillikite melt, in contrast to olivine rims in the kimberlite, where olivine crystallization typically occurred in direct response to digestion of entrained xenocrystic orthopyroxene (Russell *et*

al., 2012; Pilbeam *et al.*, 2013). Since olivine is the major silicate phase in all of these silica-undersaturated ultramafic igneous rocks, mass balance dictates that if the amount of cognate olivine is larger in aillikites, then their parental melts must have contained more SiO_2 compared to those that gave rise to kimberlites.

In the Majuagaa calcite kimberlite, Ni contents in the olivine margins rapidly decrease from ~2500 μg/g to ~1000 μg/g at relatively constant MgO/FeO (~Fo88.5), if one accounts for post-crystallization diffusion. In Ni vs. Fo diagrams for olivine margins, aillikites and mela-aillikites from West Greenland show constant Fo at ~84 % (Fig. 6), whereas the Majuagaa calcite kimberlite shows constant Fo at ~88.5 % (Nielsen & Sand, 2008; Pilbeam *et al.*, 2013, 2023). This implies lower MgO/FeO of the parental melts to the aillikites compared to the Majuagaa calcite kimberlite during olivine margin crystallization. The inferred difference in the melt MgO/FeO ratio may be even greater than indicated by the Fo values for aillikites and kimberlites because the olivine $K_D(Fe\text{-}Mg)$ is higher in more carbonate-rich melts (Dalton & Wood, 1993). This effect would amplify the relative difference in MgO/FeO between the calcite kimberlite and aillikite melts.

Crystallization of the outer olivine rims

The outer rim zone of olivine grains is thicker in the Sarfartuup Nuna South aillikites (~15 μm; up to Fo87) than in the Majuagaa calcite kimberlite (<10 μm; up to Fo94; Pilbeam *et al.*, 2013; 2023). For the Majuagaa calcite kimberlite, we argued previously that the outer rim records late-stage diffusional re-equilibration of the olivine crystals with oxidized carbonated melt (high Fe_2O_3/FeO). The outermost high-Fo rims on olivine grains in the aillikites are also consistent with such an origin. Alternatively, these rims may have formed during continuous olivine crystallization under oxidizing conditions near the FMQ buffer, known to prevail in late-stage aillikite magma (Tappe *et al.*, 2006).

Groundmass clinopyroxene

A fundamental contrast between established definitions of kimberlite on the one hand and aillikite/mela-aillikite on the other hand is the absence or presence of groundmass clinopyroxene, respectively (Tappe *et al*., 2005). Clinopyroxene, together with phlogopite, dominates the groundmass of mela-aillikite. Clinopyroxene in aillikites and mela-aillikites has characteristic Al, Ti and Fe substitutions, with Al and Fe^{3+} required to fill the tetrahedral site; and Ti^{4+}, Mg and Fe^{2+} are required to fill the octahedral site (see SI4 for more detail). The presence of groundmass clinopyroxene in the aillikite and mela-aillikite dykes, as well as the higher modal abundance of clinopyroxene in the mela-aillikites, imply an increase in αSiO_2 in melt from kimberlite through aillikite to mela-aillikite (Otto & Wyllie, 1993; Barker, 2001; Luth, 2009). In general, the compositions of clinopyroxene show consistent variations in terms of Ti, Al and Fe^{3+} both between the Sarfartuup Nuna South aillikite and the Maniitsorsuaq mela-aillikite, and within each occurrence. Ti, Al and Fe^{3+} concentrations are higher in the Maniitsorsuaq mela-aillikite clinopyroxenes than in those from the Sarfartuup Nuna South aillikite. If the silica activity coefficients are similar for both occurrences, then the higher $CaTi(AlFe^{3+})_2O_6$ component in the Maniitsorsuaq clinopyroxene reflects higher TiO_2, Al_2O_3 and Fe_2O_3 (and higher fO_2 by inference) in the melt of the mela-aillikite compared to that of the aillikite. The lower Na_2O concentration in the Maniitsorsuaq clinopyroxene is presumably a dilution effect due to the much higher modal abundance of groundmass clinopyroxene.

Phlogopite

New groundmass phlogopite EPMA data were collected for some of the aillikite and mela-aillikite dykes (Fig. 7) to complement the extensive regional dataset of Nielsen *et al.* (2009). The data (SI5) confirms the characteristic FeO_T enrichment towards the phlogopite margins for aillikites and mela-aillikites (Fig. 7b) (Tappe *et al*., 2005), as well as Ba enrichment in phlogopite margins from kimberlites (Fig. 7c) (Mitchell, 1995; Tappe *et al.*, 2014).

In addition, groundmass phlogopite was analysed in several glimmerite xenoliths from Jesper Blow (Secher *et al.*, 2009). Phlogopite from the glimmerites (SI5) has similar compositions to phlogopite cores of groundmass plates and macrocrysts (Fig. 7). Analogous to olivine, the phlogopite cores in the aillikite and mela-aillikite dykes may be xenocrystic and derived from disaggregated glimmerite xenoliths (e.g., Tappe *et al.,* 2006). Alternatively, the glimmerites are glomerocrysts similar to those found in some carbonatites (e.g., Seifert *et al.,* 2000; Reguir *et al.*, 2009). Currently, we cannot distinguish between these options. However, a non-cognate origin for the glimmerite xenoliths and, by extension, some of the phlogopite cores in the aillikites, appears likely given the increasing abundance of mica and glimmerite xenoliths from the Maniitsoq region in the south to the Sisimiut region in the north (Garrit, 2000; Larsen & Garrit, 2005). Such micaceous xenoliths have been linked to an isotopically enriched ancient mantle component (Tappe *et al*., 2011a). We note, however, that not all phlogopite cores in aillikites and mela-aillikites show disequilibrium textures of the kind described above.

The characteristically elevated BaO contents of phlogopite margins in kimberlites (e.g., Mitchell, 1995; Tappe *et al*., 2005) may be explained by the relative modal abundances of groundmass phlogopite. The amount of groundmass phlogopite increases from <1 vol.% in the Majuagaa calcite kimberlite dyke to 3-5 vol.% in the Maniitsorsuaq mela-aillikite. Hence, Ba may simply be more diluted in the more abundant phlogopite that typifies aillikites at similar bulk-rock Ba concentration levels (to kimberlites), which assumes lack of other major Ba-bearing mineral phases.

Apatite

Fluorapatite is a ubiquitous liquidus phase in the calcite kimberlites and aillikites of southern West Greenland (Table 2, SI6). Apatite from the Majuagaa calcite kimberlite has variable contents of Na_2O (3.4 wt.% down to detection limits at 0.02 wt.%), SiO_2 (<0.15 wt.%), SrO

(<1 wt.%) and LREE (<2100 μg/g La; <4400 μg/g Ce). No obvious compositional differences were identified between type 1 and type 2 apatite, except that the latter tends to have higher Na_2O. The enrichment in Na is inconsistent with the low bulk-rock Na contents of the Majuagaa calcite kimberlite. However, the Na_2O contents of olivine-hosted melt inclusions in the Majuagaa calcite kimberlite are also considerably higher than in the bulk-rock (Kamenetsky *et al.,* 2009). This suggests that Na_2O may have been lost to a fluid phase in a manner analogous to fluid-driven alkali metasomatism (fenilization) during carbonatite magma emplacement (Harmer & Gittins, 1997; Veksler & Keppler, 2000; Keppler, 2003; Soltys et al., 2018; Yaxley *et al.,* 2022).

The elevated Na content in apatite from the Majuagaa calcite kimberlite correlates with low sums for elements that typically occupy the phosphorous-site (Fig. 8a). This is probably due to coupled substitution between Na^+ at the Ca-site and CO_3^{2-} at the P-site (McClennan & Lehr, 1969; Pan & Fleet, 2002). Carbonate-bearing apatite is known from experimental carbonatitic systems (e.g., Fleet & Liu, 2007; Hammouda *et al*., 2010), but also from naturally occurring rocks (Soltys *et al.,* 2020b). For the Majuagaa calcite kimberlite, a high carbonate content of groundmass apatite may record high CO_2/SiO_2 of the parental melt.

Apatite in the aillikites from P-Dyke, Jesper blow, Sarfartuup Nuna South and Maniitsorsuaq has low Na_2O (<0.2 wt.%), up to 3 wt.% SiO_2, relatively low SrO (<1 wt.%) and low LREE (La and Ce) compared to groundmass apatite in the Majuagaa calcite kimberlite (Table 2). Apatite from these occurrences is similar in composition to groundmass apatite in the Torngat aillikites and mela-aillikites (Tappe *et al.,* 2004). Silicon resides in the P-site, which is fully occupied in our three aillikite occurrences (Fig. 8b). Importantly, SiO_2-bearing apatite from the aillikites may record lower CO_2/SiO_2 of the parental melt, in contrast to the Majuagaa calcite kimberlite melt.

Silicon is lower in apatite from the Maniitsorsuaq mela-aillikite than in apatite from the transitional P-Dyke and the Sarfartuup Nuna South aillikite dyke. The same is observed

in the Torngat ultramafic lamprophyres of northern Labrador (Tappe *et al*., 2004). The observation appears to be in conflict with evidence from higher groundmass clinopyroxene and cognate olivine contents in the mela-aillikites demonstrating higher SiO_2 in the parental melt. However, experiments show that the SiO_2 content in apatite can decrease with increasing SiO_2 in coexisting silicate melts (Prowatke & Klemme, 2006), whereas Si is partitioned into apatite in carbonatitic melts (Dawson & Hinton, 2003). Also, late-stage CO_2 degassing has also been considered as a link between coeval aillikites and mela-aillikites (Tappe *et al.,* 2006).

The La and Ce concentrations in apatite in the ultramafic lamprophyres are relatively low compared to apatite in the Majuagaa calcite kimberlite (Fig. 8c), which is a key observation because the bulk rock LREE contents in kimberlites and aillikites are similarly high. Partition coefficients for La and Ce in apatite in equilibrium with silicate melts are in the range 4-16 (Prowatke & Klemme, 2006), which is much higher than apatite/melt K_D values for LREE in carbonate systems (0.2-0.7; Klemme & Dalpé, 2006) (see also Fig. 12 of Hammouda *et al.*, 2010). Partition coefficients for La and Ce in perovskite are in the range 2-5 in kimberlites and aillikites with high $CaO+MgO/SiO_2+Al_2O_3$ (Beyer *et al*., 2013). The lower LREE contents of apatite from aillikites compared to those from kimberlites probably reflect LREE depletion in remaining melt after early perovskite crystallisation. This agrees with Jones & Wyllie (1984) who also found that the LREE preferentially partition into perovskite when coexisting with apatite in kimberlitic rocks.

Groundmass apatite in the Majuagaa calcite kimberlite, as well as in the transitional P-Dyke and Sarfartuup Nuna South aillikite is characterized by almost complete anion site occupancy by fluorine (Table 2). In contrast, the anion site in groundmass apatite from the Maniitsorsuaq mela-aillikite contains F and OH in approximately equal amounts, similar to apatite in kimberlites from Lac de Gras in Canada (Chakhmouradian *et al.*, 2002). This may imply elevated αH_2O in the mela-aillikite magma compared to the other Greenland

603 occurrences. However, Tappe *et al.* (2004) reported an opposite pattern for apatite from the
604 Torngat ultramafic lamprophyres in northern Labrador, with 1.25-2 wt.% F in aillikitic and
605 up to 3 wt.% F in mela-aillikitic apatite.

606 **Perovskite**

607 Perovskite is very rare in the Majuagaa calcite kimberlite, compared to its ubiquitous
608 occurrence in the groundmass of aillikites (Sarfartuup Nuna South) and mela-aillikites
609 (Maniitsorsuaq) (see also Nielsen *et al.,* 2009; Tappe *et al.,* 2012). Representative analyses
610 are reported in Table 3 and the full dataset is found in file SI7. In general, Nb–Na–LREE
611 contents are elevated in groundmass perovskite from all rock types and occurrences studied.

612 **Calcite**

613 Electron microprobe analyses of calcite from the mesostasis of the Majuagaa calcite
614 kimberlite, the Sarfartuup Nuna South aillikite and the Maniitsorsuaq mela-aillikite are listed
615 in Table 4 and SI8. The Sr content of calcite at Majuagaa varies between the detection limit
616 and 3300 μg/g. In aillikites, groundmass calcite is generally richer in Sr (2000-6000 μg/g)
617 compared to the Majuagaa calcite kimberlite, but lower than in the mela-aillikites (up to 1.5
618 wt.% SrO). Ba content in calcite varies between the detection limit and 1400 μg/g for all
619 three ultramafic dyke occurrences. The elevated Sr and Ba contents support a magmatic
620 origin for groundmass calcite (Exley & Jones, 1983), in line with our interpretation of
621 primary magmatic textures for the carbonates in the Majuagaa kimberlite dyke (e.g.,
622 exsolution textures; Figs 3a-b). The increase of Sr in groundmass carbonates from calcite
623 kimberlite through aillikite to mela-aillikite probably reflects mass balance with decreasing
624 modal calcite abundances, as well as Sr enrichment in the late-stage residual melt fractions.
625

626 **Summary of petrographic and mineralogical interpretations**
627
628 The textural and mineral compositional data presented above have implications for our

interpretations and guide the modeling of the bulk rock geochemical data presented below.

The mineralogical observations can be summarized as follows:

1. Sorting of xenoliths and megacrysts within individual dyke intrusions is evident as variable mineral proportions across dykes caused by flow differentiation during magma ascent and emplacement. The proportion of glimmerite xenoliths increases from the craton interior at Maniitsoq (e.g., the Majuagaa calcite kimberlite dyke) towards the craton margin at Sarfartoq (e.g., Nielsen *et al*., 2009) and farther into the Proterozoic mobile belt at Sisimiut.
2. For all occurrences studied, olivine cores have compositions similar to olivine from cratonic peridotite xenoliths, which supports the non-cognate (xenocrystic) origin for the cores of many olivine grains from kimberlites, aillikites and mela-aillikites. The small groundmass olivine crystals reveal the full range of compositions known from larger zoned olivine grains. The magmatic olivine crystallization onto the non-cognate olivine cores was relatively homogenous. Grain fragmentation continued after olivine crystallization had ceased.
3. A higher proportion of olivine in the ultramafic lamprophyres is cognate compared to the Majuagaa calcite kimberlite. This implies that the aillikites and mela-aillikites formed from more SiO_2-rich parental melts than the Majuagaa calcite kimberlite. The lower Fo values for the cognate olivine in aillikites compared to magmatic olivine in kimberlite also implies lower MgO/FeO_T in the aillikites and mela-aillikites.
4. The increasing groundmass clinopyroxene content (from absent in kimberlite to dominant in mela-aillikite) implies higher αSiO_2 for the ultramafic lamprophyre magmas at emplacement level relative to the Majuagaa calcite kimberlite. TiO_2 and Al_2O_3 contents are highest in the mela-aillikite clinopyroxene, which may imply

higher Ti and Al contents in the mela-aillikite parental melt.

5. The proportion of groundmass phlogopite increases from very low in calcite kimberlite to dominant in mela-aillikite. This reflects higher magmatic H_2O and melt K_2O contents in the ultramafic lamprophyres than in the calcite kimberlite. Some groundmass phlogopite cores show petrographic evidence for disequilibrium with the surrounding melt and exhibit a compositional overlap with phlogopite from glimmerite xenoliths. They may be derived from the disaggregated glimmerite xenoliths during magma ascent.

6. The Si content of apatite changes from low in the calcite kimberlite to high in the aillikites, which suggests variable melt SiO_2/CO_2. Na contents of groundmass apatite, clinopyroxene and perovskite are high with respect to the bulk rock compositions, which implies fluid-related mobilization of Na from the ultrabasic magmas.

BULK ROCK GEOCHEMISTRY

We report 28 new bulk rock major and trace element analyses including CO_2 contents for samples from three ultramafic lamprophyre occurrences in southern West Greenland (Table 5a and b and SI9). In addition, we determined the CO_2 contents of seven aillikite samples from Sarfartuup Nuna South, for which major and trace element data were previously reported by Nielsen *et al. (*2009).

Maniitsorsuaq mela-aillikite

For the Maniitsorsuaq mela-aillikite samples (Table 5a), the contents of Al_2O_3, CaO, K_2O, Sc, Rb and Ba (not shown) decrease with increasing MgO, whereas Ni and Cr contents increase (Fig. 9). SiO_2 decreases slightly with increasing MgO. These variations in major and compatible trace element concentrations reflect the variation in modal proportions between

683 samples. The main geochemical trends identified in Figure 9 can be explained by higher
684 modal proportions of phlogopite (Al_2O_3, K_2O, Rb, Ba) and clinopyroxene (SiO_2, CaO, Sc) in
685 some samples, and higher olivine (MgO, Ni) and Cr-spinel (Cr) in others. The small decrease
686 in SiO_2 with increasing MgO reflects the higher SiO_2 contents of phlogopite and diopside-
687 rich clinopyroxene compared to olivine. Given that Nb, P_2O_5 and CO_2 are largely contained
688 in perovskite, apatite and calcite respectively, these elements show no consistent variation
689 with the modal proportions of olivine, clinopyroxene and phlogopite.
690 The samples with larger amounts of modal olivine and lower amounts of phlogopite
691 and clinopyroxene typically derive from the massive central portions of relatively thick
692 dykes (e.g., 517910). In contrast, samples with large amounts of modal phlogopite and
693 clinopyroxene stem typically from their flow-banded margins (e.g., 517905). This change in
694 the modal proportions, also apparent at thin section scale, is primarily caused by flow sorting
695 of the crystalline material during emplacement. It is an important process in kimberlites and
696 related rocks as it affects the bulk compositions of individual samples (Mitchell, 2008; Tappe
697 *et al.*, 2014). Phlogopite and clinopyroxene crystallized *in-situ* from the melt at the mela-
698 aillikite dyke margins, and their apparent higher modal abundances relative to the dyke
699 interiors are due to flow concentration of olivine macrocrysts and xenoliths in the central
700 parts of the dykes (Fig. 2a).

701 **Sarfartuup Nuna South aillikite**
702
703 In the Sarfartuup Nuna South aillikite (Table 5b), SiO_2, Ni and Co increase whereas Al_2O_3,
704 CaO, K_2O, P_2O_5, CO_2, Sc, Rb and Sr decrease with increasing MgO (Fig. 10). The H_2O
705 content is slightly elevated in some samples due to serpentinization, which has no systematic
706 impact on the chemical elements of interest in this study. As illustrated by the mineral
707 control lines in Figure 10, the main geochemical trends are consistent with higher modal
708 amounts of olivine in some samples (higher SiO_2, MgO, Ni, Co), as opposed to higher modal

amounts of phlogopite (K_2O, Al_2O_3, Rb), clinopyroxene (CaO, Sc), apatite (P_2O_5) and calcite (CaO, CO_2, Sr) in other samples.

The samples from this aillikite occurrence are largely subcrop and no control is possible upon their relative position in the dyke. However, evidence from several other volatile-rich ultramafic dyke occurrences in southern West Greenland suggests that these linked modal and geochemical variations are mainly due to concentrations of olivine macrocrysts towards dyke interiors with melt components flowing and segregating along the dyke margins (e.g., Pilbeam *et al.,* 2023). Increasing SiO_2 contents with increasing MgO, rather than increasing CaO as in the Maniitsossuaq occurrence, reflect the lower modal proportion of clinopyroxene in aillikite compared with mela-aillikite, which in turn suggests a lower melt SiO_2 content in the aillikite magma at emplacement level (see also Tappe *et al.,* 2004).

P-Dyke

The P-Dyke shows relatively little variation in the concentrations of most major elements (Table 5b). The dyke manifests itself only as subcrop and it is therefore impossible to assess whether samples come from the interior or margins of the dyke. The samples show a weak correlation between the MgO and Ni contents indicative of variable olivine proportions. The H_2O content is generally high, recording pronounced serpentinization.

CONSTRAINTS FOR A MIXING MODEL

Evaluation of the effects of flow differentiation

The modeling of compositional trends for discrete dykes and for the suite of melt types in southern West Greenland requires an evaluation of processes and factors that may have had an influence on the magma compositions during emplacement in the upper crust. The two main complications are flow differentiation and the proportion of entrained lithospheric

mantle components.

Olivine grains in kimberlites and related rocks are typically composite with xenocrystic cores and cognate overgrowths (Fedortchouk & Canil, 2004; Nielsen & Sand, 2008; Brett *et al.*, 2009; Bussweiler *et al.,* 2015; Giuliani, 2018; Shaikh *et al.,* 2021; Pilbeam *et al.*, 2023; our Figs. 5 and 6). Textural observations of fractured olivine grains, abraded olivine grain margins, and overlap in compositions between unzoned groundmass olivine and zoned olivine macrocrysts imply that crystal cargo transport continued after crystallization of the olivine margins (Brett *et al.*, 2009; Arndt *et al.*, 2010). In kimberlites, including the calcite kimberlite variety such as the Majuagaa dyke, cognate olivine margins form in response to orthopyroxene xenocryst dissolution (Pilbeam *et al*., 2013). In addition to orthopyroxene dissolution, other mantle phases such as disc-shaped pyrope-rich garnets (Nielsen & Jensen, 2005) may also be assimilated by ascending kimberlite magmas, further modifying melt compositions (e.g., Canil & Fedortchouk, 1999). Phases that crystallize relatively early such as Cr-spinel and perovskite may have been sorted during magmatic flow similar to the olivine macrocrysts.

The fundamental implication of the above observations is that kimberlitic melts are emplaced at crustal levels as a complex hybrid magmatic mixture, and do not have the same major element bulk compositions as melts near the mantle source within the lithosphere–asthenosphere transition zone (see also Soltys et al., 2018). The observed bulk compositional arrays for each kimberlite or aillikite occurrence studied in West Greenland are indicative of unmixing of the ultramafic magmas, with xenocrysts and early crystallizing materials being concentrated in the dyke interiors, and the transporting melt being concentrated near the dyke margins. Since the olivine grain populations in the dyke interiors include cognate crystals, the samples with low olivine macrocryst contents at the dyke margins (so-called aphanitic kimberlites) cannot represent a progression towards the parental melt but rather towards the ‘emplacement melt’. Thus, bulk rock arrays cannot be projected towards a

potential parental melt composition, an approach taken in many kimberlite studies (le Roex *et al.,* 2003; Kjarsgaard *et al.*, 2009; Tappe *et al.*, 2017a). Aphanitic samples such as 491716 from Majuagaa or 517905 from Maniitsorsuaq, as well as those studied by Price *et al*. (2000) from Canada, do not necessarily represent primitive melt compositions.

To understand the bulk compositions of kimberlites and aillikites from West Greenland (and elsewhere) it is thus imperative to investigate representative suites of samples from each occurrence. The underlying assumption is that the average composition of each suite represents a mixture of melts and fragments derived from the deep SCLM, as well as assimilated components. In the mixing model developed below, it is also assumed that the average analytical bulk rock composition of a suite of samples is the same as that of the given batch of kimberlites or aillikites as they rose from the mantle source region. When making this assumption, we are excluding wall rock reactions after magma ascent has started, and also loss of crystalline material during upwards migration of the magma from the lithosphere–asthenosphere transition zone to its final emplacement within the continental crust. Russell and Jones (2023) argue for possible decoupling of melt components and solid cargo due to lagging effects, but the loss of significant proportions of crystalline material can presumably be excluded for the ultramafic dykes from West Greenland. They transported 30 to 60 vol.% of crystals and xenoliths from most parts of the lithospheric mantle (Sand, 2007; Sand *et al.*, 2009), and their emplacement is best compared to laminar flow of liquid concrete (Fig. 2).

We cannot entirely exclude reaction between the intruding kimberlite and aillikite mushes and surrounding lithosphere *en route* from the mantle source to final emplacement. But detailed modeling of the possible amount of interaction with wall rocks requires modeling of the physical characteristics of the heterogeneous mushes as well as possible magma ascent rates and very detailed information on processes *en route* (e.g., Giuliani et al., 2013; Soltys et al., 2020a). Such modeling is beyond the scope of the present study, and in

our modeling we assume only insignificant reaction between the SCLM and the rising magmas *en route* to crustal emplacement levels.

Evaluation of bulk rock geochemical trends

The major element compositions of the three aillikite dyke occurrences and the Majuagaa calcite kimberlite dyke are displayed in a series of element–element plots (Fig. 11). We also include the fields of the compiled dataset of Nielsen *et al.,* (2009) and the data from Tappe *et al.* (2011a) for southern West Greenland, as well as data for the similarly aged Torngat aillikites and mela-aillikites from the Canadian margin of the Labrador Sea rift (Tappe *et al*., 2004, 2008). Broadly, SiO_2, TiO_2, Al_2O_3, FeO_T, K_2O, Sc, V and Rb increase, and MgO, CO_2, Ni decrease from calcite kimberlites through aillikites to mela-aillikites in the Late Neoproterozoic Greenland–Labrador Diamond Province (Tappe *et al.,* 2014). CaO and Co are approximately steady across the range of magma types. Although the compositional fields of all three rock types show considerable overlap, there are some notable differences. The transitional P-Dyke in particular has lower contents of TiO_2, Al_2O_3, CaO and K_2O than the Greenland calcite kimberlites (Nielsen *et al.,* 2009), whereas the Majuagaa calcite kimberlite dyke has even higher TiO_2 than all the other kimberlites from West Greenland due to a high abundance of ilmenite megacrysts (Nielsen & Sand, 2008; Pilbeam *et al*., 2023).

The compositional spread in Fig. 11 illustrates clearly the widely recognized difficulties in using bulk rock major element compositions to examine these volatile-rich ultramafic magma types (e.g., Mitchell & Tappe, 2010). The main reason for these diagrams being difficult to interpret reflects the combined effects of each dyke occurrence containing a different proportion of entrained mantle material. Each sample from a given occurrence records a different degree of flow differentiation with respect to the abundance of olivine macrocrysts and other crystal cargo. None of the bulk rock major element compositions can

be considered to represent a liquid composition (see also Giuliani *et al.*, 2020). It must be noted that the apparent ability of statistical methods (e.g., PCA) to discriminate between kimberlite magma types is misleading because results are not reproducible at the regional or global scale (e.g., Grunsky & Kjarsgaard, 2008). Therefore, to evaluate the bulk rock major and minor element compositions we take a similar approach to that in Pilbeam *et al.* (2023), with geochemical compositions being treated as dynamic mixtures between a melt component and solid entrained mantle components.

Ni in melt in the SCLM will always be buffered as long as olivine is present in the mantle source residue. Olivines from the West Greenland SCLM have a limited compositional range with most olivines ranging from 90-93 % Fo at 3000 ppm Ni, decreasing to 86 % Fo at 2000 μg/g Ni in dunites (Fig. 5). Because the variations in the SCLM are so limited and because the Mg# of the analysed phlogopite is similar to that of primitive kimberlite melts worldwide (Giuliani et al., 2020), the main variation observed in Figure 12 cannot be due to variation in the compositions of xenocrystic olivine. Nor can it be due to assimilation of phlogopite-rich mantle rocks. We therefore argue that this variation is a direct function of contributions from entrained refractory materials from the SCLM. Figure 12 shows that the calcite kimberlites from Maniitsoq on the North Atlantic Craton contain a higher proportion of refractory mantle material than the aillikites from farther north in West Greenland and northern Labrador. Note that for a specific dyke, the MgO/Ni ratio is controlled by accumulation of olivine, which represents both the entrained xenocrystic mantle component and magmatic olivine. This explains the oblique array of samples in the Ni vs. MgO diagram (Fig. 12). All these samples originate from the Majuagaa dyke (Nielsen *et al.*, 2009), which represents a carbonate-rich kimberlite endmember (Pearson *et al.*, 2019). Following Pilbeam *et al.* (2013, 2023), olivine margins crystallize from a melt at the expense of orthopyroxene. Ni is limited to <1000 μg/g in dissolved orthopyroxene (Nielsen & Jensen, 2005) and the magmatic olivine margins inherited low Ni.

Following the above argument that variations in bulk MgO content are largely due to a variable proportion of entrained xenocrystic mantle component, we can use ratios between elements and MgO as a qualitative proxy for melt composition. The approach is similar to that of Pearce (2008) for basaltic magmas. Figure 13 displays the variations in melt compositions from the Maniitsoq kimberlites through the southern West Greenland aillikites/mela-aillikites to the Torngat aillikites/mela-aillikites from northern Labrador. In our view, the increases in SiO_2/MgO, TiO_2/MgO, Al_2O_3/MgO, FeO_T/MgO, Na_2O/MgO, K_2O/MgO, and decrease in CO_2/MgO across West Greenland to northern Labrador record compositional variations of the magmas at emplacement level. Deviations from these trends are exhibited by the CaO and H_2O systematics. The CaO concentrations are similar across the province (Table 5a and b), but the CaO/MgO is at a given SiO_2/MgO systematically elevated in the aillikites compared to the mela-aillikites (Fig. 13d), whereas H_2O/MgO is variably low in the kimberlites (Fig. 13f).

The general geochemical and petrographic progression outlined above is in contrast to the hypothesis that carbonatites, aillikites and kimberlites form a magma series with increasing melt SiO_2 contents reflecting increasing degrees of partial melting of a similar mantle source (e.g., Dalton & Presnall, 1998a). The SiO_2 content is higher in the aillikite melt compared to calcite kimberlite, as also evidenced by the presence of groundmass clinopyroxene in aillikites and its absence in kimberlites (Tappe *et al.*, 2005). Higher silica activity of aillikite and mela-aillikite melts compared to archetypal kimberlite melt is the most plausible explanation (Otto & Wyllie, 1993; Barker, 2001; Luth, 2009).

H_2O contents are highly variable within individual dyke occurrences due to variations in the extent of serpentinization, which may be caused by juvenile and meteoric fluids, as well as degassing and losses during reactions with crustal host rocks (e.g., Mitchell, 2013). However, mass balance of K_2O and H_2O suggests that there is an overall higher original K_2O and thus H_2O content in the aillikites compared to the calcite kimberlites. This H_2O is

868 structurally bound in phlogopite of magmatic origin and might approximate the original H_2O
869 content in the melt. Alternatively, it may be constrained by SiO_2 and K_2O contents as
870 required for phlogopite stabilization in the melt. The similarly normalized compositions for
871 compatible elements (Sc, V, Cr and Co) are shown in Figure 14.
872 The normalized multi-element plots demonstrate the overall similarity of the
873 incompatible trace element patterns for aillikites and mela-aillikites and the Majuagaa calcite
874 kimberlite dyke (Fig. 15). The Torngat aillikites and mela-aillikites from northern Labrador
875 have on average 2 to 3 times higher trace element concentrations compared to the tight
876 groups of the Greenland dykes. There are, however, important compositional differences
877 among the Greenland occurrences, in particular the higher Hf (Fig. 15) and Rb, Zr (Fig. 16b
878 and c) contents of the aillikites/mela-aillikites in comparison to the calcite kimberlites. The
879 element ratio vs. SiO_2/MgO plots (Fig. 16g-h) also demonstrate that the lower incompatible
880 element concentrations of the Greenland occurrences compared with those from Labrador
881 are not related to a difference in the ratios between very incompatible and moderately
882 incompatible element ratios (VICE/MICE). The lower but increasing concentrations of
883 incompatible trace elements in the West Greenland kimberlites and aillikites compared to
884 those from northern Labrador are presumably due to the involvement of a much more
885 enriched component in the mantle source beneath the Torngat Mountains. The trend in bulk
886 rock trace element compositions from the Maniitsoq calcite kimberlites to Sarfartoq aillikites
887 and Sisimiut mela-aillikites, and highly-enriched aillikites and mela-aillikites from northern
888 Labrador, was identified previously, albeit on the basis of fewer data (Tappe *et al.*, 2008;
889 Nielsen *et al.*, 2009; Tappe *et al.*, 2011a).
890

891 **MODEL FOR THE RELATIONSHIPS BETWEEN CARBONATITE,**
892 **KIMBERLITE AND AILLIKITE**

893 Given the spatiotemporal association and the largely consistent regional geochemical trends

894 described so far, a petrogenetic link may exist between the calcite kimberlite and
895 aillikite/mela-aillikite occurrences in West Greenland (Nielsen *et al.*, 2009; Tappe *et al.*,
896 2011a, 2017b). In Pilbeam *et al.* (2023), we established that the Majuagaa calcite kimberlite
897 can be explained by involvement of a very carbonate-rich melt component generated by
898 low-degree partial melting of a mantle source with overall REE concentrations similar to
899 those of primitive mantle, plus entrainment of mantle materials in the form of xenocrysts
900 and variably reacted xenoliths. Melting experiments in CO_2-bearing peridotite systems at 3-
901 8 GPa show that melts close to the solidus are carbonatitic (Dalton & Presnall, 1998a;
902 Dasgupta & Hirschmann, 2007) and that the SiO_2 content increases with progressive
903 melting, becoming more similar to silicate melts at the CO_2-absent solidus (e.g., Dalton &
904 Presnall, 1998b; Gudfinnsson & Presnall, 2005; Brey *et al.*, 2008; Foley *et al.*, 2009, 2019).
905 If melting occurs by either the batch or fractional melting mechanism, with instantaneous
906 equilibration between melt and source, then the concentration of VICE and VICE/MICE
907 ratios will decrease as the melt proportion increases (Shaw, 1970).

908 The major element and compatible trace element variations in the melts of the aillikite
909 and mela-aillikite occurrences in West Greenland and northern Labrador, as they rose from
910 their source area in the subcontinental lithosphere, can be reconciled with variations in the
911 degree of partial melting of similar source materials. The incompatible trace element
912 signatures require an additional source component for Labrador. However, the overall
913 VICE/MICE enrichments are similar for the three aillikite occurrences and the Majuagaa
914 calcite kimberlite dyke (Figs. 15-16), despite the notably different melt major element
915 compositions and differences in Zr–Hf. One way to reconcile these data is to invoke
916 differences in the contributions to the magmas from the entrained xenolith assemblages. The
917 proportion of glimmerite xenoliths increases northwards from virtually absent in the
918 Majuagaa calcite kimberlite to prominent in the Maniitsorsuaq mela-aillikite (Garrit, 2000;
919 Larsen & Garrit, 2005). The geochemical and Nd–Hf isotope data of Tappe *et al.* (2008,

920 2011a) suggest that the Labrador aillikites and mela-aillikites are the result of interactions
921 between an asthenospheric carbonate-rich silicate melt and melts derived from K-rich
922 metasomes in the cratonic mantle lithosphere. The same is suggested for Sarfartoq aillikites
923 including Sarfartuup Nuna South, but with a significantly smaller proportion of K-rich SCLM
924 component.

925 Simple mass balance shows, however, that wholesale entrainment of glimmerite,
926 analogous to that of the refractory peridotitic component (Pilbeam *et al*., 2013), cannot
927 explain the extent of the raised K_2O contents of the aillikites and mela-aillikites in West
928 Greenland or Labrador. Importantly, melting experiments on phlogopite-bearing peridotite
929 assemblages show that the increased presence of alkalis lowers the solidus (Dasgupta &
930 Hirschmann, 2007; Foley *et al*., 2009) and results in higher melt SiO_2 at a given temperature,
931 pressure and melting degree (Foley *et al.*, 2009). In addition, phlogopite is stable at low CO_2
932 conditions at lithospheric mantle pressures (Kushiro *et al*., 1967), but the peridotitic mantle
933 solidus is lowered considerably by the presence of carbonates (Ulmer & Sweeney, 2002).
934 Mixed phlogopite–carbonate assemblages are unstable at >200 km depth along a cratonic
935 geotherm of ~40 mWm^{-2} (Enggist *et al*., 2012), which is relevant to the deep lithospheric root
936 beneath West Greenland at ca. 600-550 Ma (Sand *et al.*, 2009). If a carbonate-rich silicate
937 melt from the asthenosphere infiltrates a lithospheric mantle section that is extensively veined
938 by phlogopite-rich metasomes, then melting of phlogopite will occur (Tappe *et al.*, 2008).
939 Melting of pure phlogopite metasomes would be incongruent (Yoder & Kushiro, 1969;
940 Modreski & Boettcher, 1973) and produce residual olivine (e.g., Rooney *et al.*, 2020), which
941 would result in SiO_2 contents that are too low for aillikites. However, this effect may be offset
942 by extra silica in consequence of a depressed mantle solidus and increased melting of
943 clinopyroxene and/or olivine.

944 Here, we propose that the metasomatic component identified in aillikites and mela-
945 aillikites stems from partial melting of a phlogopite–clinopyroxene assemblage (known to

946 occur as a xenolith type in aillikites from Labrador; Tappe *et al.*, 2006), or alternatively from
947 melting of phlogopite metasomes joined by partial melting of clinopyroxene-bearing
948 peridotitic wall-rock (e.g., Foley, 1992). The model in Figure 17 compares the compositions
949 of the four studied occurrences and mixing models between three components: (1) the
950 primary carbonate-rich Majuagaa melt (Pilbeam *et al*., 2023) derived by low-degree partial
951 melting of asthenospheric mantle in the presence of CO_2; (2) a refractory garnet harzburgite
952 component representative of a common West Greenland lithospheric mantle contaminant
953 (Pilbeam *et al*., 2023); and (3) an experimental melt of a 1:1 clinopyroxene and phlogopite
954 vein assemblage (Foley *et al.*, 1999). Mixing between these three components can explain the
955 SiO_2, Al_2O_3, FeO_T, MgO, CaO and K_2O variations observed for the four ultramafic dyke
956 occurrences studied. Examples of the modeling, including the endmember proportions and
957 the resulting model melt compositions, are listed in Table 6.

958 The transitional P-Dyke melt is very similar to the Majuagaa calcite kimberlite melt,
959 but with a higher proportion of the harzburgite endmember and only a minor melt
960 contribution from the clinopyroxene–phlogopite metasome. In terms of major elements, the
961 Maniitsorsuaq mela-aillikite is strongly influenced by melt from the clinopyroxene–
962 phlogopite metasome. The Sarfartuup Nuna South aillikite is intermediate between the
963 Maniitsorsuaq mela-aillikite and the Majuagaa calcite kimberlite. However, a misfit exists
964 between the modeled average and observed aillikite compositions, mainly concerning the
965 contribution from the metasome-derived melt component. The deviations are most
966 pronounced for K_2O, Al_2O_3 and FeO_T, which suggests an overestimation of the proportion
967 of the inferred metasomatic mantle source component.

968 In summary, our modelling is consistent with the hypothesis that the elemental
969 variations between calcite kimberlite and aillikites in West Greenland are largely controlled
970 by the relative contributions from diverse lithospheric mantle lithologies, with aillikites
971 exhibiting incorporated components from phlogopite-bearing lithologies that appear to be

absent or rare in the SCLM farther south. We note that our conclusions, although based on a different approach utilizing mineral and whole rock compositions, are consistent with and independently confirm the conclusions of Tappe et al. (2011a), which were supported by modeling of bulk rock Nd-Hf isotope data. However, the amounts of the various components required to explain the observed variations in West Greenland are quite different, because the two approaches rely on partly deviating assumptions regarding the exact nature of the mixing endmembers. Further reconciliation of the quantitative petrogenetic models is the subject of ongoing research.

CONCLUSIONS

Regardless of some discrepancies, bulk-rock modeling demonstrates that the observed variations in the major and trace elements and isotopic ratios of the Neoproterozoic kimberlites, aillikites and mela-aillikites from West Greenland and northern Labrador can be reconciled within a unified petrogenetic scheme. From Maniitsoq in West Greenland to the Torngat Mountains in northern Labrador, melt derived from phlogopite–clinopyroxene metasomes was added in increasing proportions to regionally widespread deep-sourced carbonate-rich silicate melts that carried a solid cargo of refractory mantle materials (Tappe *et al.,* 2008, 2011a, 2012; Nielsen *et al.,* 2009; Pilbeam *et al.,* 2023). In addition we conclude that:

1) The bulk rock arrays of individual volatile-rich ultramafic dyke occurrences of kimberlitic affinity reflect variable proportions of crystalline material in carrier melt, with magma flow-induced unmixing between the melt component and genetically complex olivine macrocrysts.
2) The proportion of entrained lithospheric mantle material is variable for each locality studied in West Greenland, and across the entire kimberlite–aillikite–carbonatite

province including Labrador.

3) Points 1 and 2 above make interpretations of individual bulk rock analyses difficult because none of them represent liquid compositions. This issue can be circumvented by using ratios of selected elements over MgO for qualitative comparisons between kimberlite and aillikite occurrences.
4) Variations in petrography and mineral compositions between calcite kimberlites and aillikites/mela-aillikites record systematic differences in the major element compositions of the respective parental melts, which formed in the asthenosphere and heterogeneously metasomatized cratonic mantle lithosphere.

FUNDING

Funding for the project was provided by Geocenter Denmark project (6-2007) and GEUS.

DATA AVAILABILITY

All data used in this study are included in tables and supplementary information and cited works.

SUPPLEMENTARY DATA

Supplementary data are available at Journal of Petrology online.

ACKNOWLEDGMENTS

This study is part of a Ph.D. study carried out last decade at the University of Copenhagen and the Geological Survey of Denmark and Greenland (GEUS). Alfons Berger is thanked for excellent advice and support obtaining microprobe data. ST acknowledges the Faculty of Science and Technology at UiT for supporting Solid Earth research topics. Susanne Rømer

is thanked for much help with the illustrations. We thank Lynton Jaques and two anonymous reviewers for their constructive comments, and Marlina Elburg and Georg Zellmer for editorial handling.

REFERENCES

Abersteiner, A., Kamenetsky, V.S., Goemann, K, Golovin, A. & Kamenetsky, M. (2022). Olivine in Kimberlites: Magma Evolution from Deep Mantle to Eruption. *Journal of Petrology* **63**, 1-32. https://doi.org/10.1093/petrology/egac055.

Arevalo, R. & McDonough, W. F. (2010). Chemical variations and regional diversity observed in MORB. *Chemical Geology* **271**, 70-85. https://doi.org/10.1016/j.chemgeo.2009.12.013.

Arndt, N. (2003). Komatiites, kimberlites, and boninites. *Journal of Geophysical Research* **108**, 2293-2304. https://doi.org/10.1029/2002JB002157.

Arndt, N. T., Guitreau, M., Boullier, A. M., Le Roex, A., Tommasi, A., Cordier, P. & Sobolev, A. (2010). Olivine, and the origin of kimberlite. *Journal of Petrology* **51**, 573-602. https://doi.org/10.1093/petrology/egp080.

Arndt, N., Cordier, C., Boullier, A.-M., Batanova, V. Magnin, V. & Findling, N. (2022). Olivine in kimberlites and related rocks – macrocrysts, dunitic xenoliths and megacrysts from the same metasomatized source. *Journal of Petrology* **63**, 1–20. https://doi.org/10.1093/petrology/egac063.

Aulbach, S., J. Sun, J., Tappe, S. & Gerdes, A. (2019). Effects of multi-stage rifting and metasomatism on HSE - 187Os/188Os systematics of the cratonic mantle beneath SW Greenland. *Contributions to Mineralogy and Petrology* **174** (2), 1-16. https://doi.org/10.1007/s00410-019-1549-7.

Aulbach, S., Sun, J., Tappe, S., Höfer, H.E., Gerdes, A. (2017). Volatile-rich metasomatism in the cratonic mantle beneath SW Greenland: Link to kimberlites and mid-lithospheric discontinuities. *Journal of Petrology* **58**, 2311-2338. 10.1093/petrology/egy009.

Barker, D. S. (2001). Calculated silica activities in carbonatite liquids. *Contributions*

to Mineralogy and Petrology 141, 704-709. https://doi.org/10.1007/s004100100281.

Becker, M. & le Roex, A. P. (2006). Geochemistry of South African on and off-craton, Group I and Group II kimberlites: petrogenesis and source region evolution. *Journal of Petrology* **47**, 673-703. https://doi.org/10.1093/petrology/egi089.

Beyer, C., Berndt, J., Tappe, S., Klemme, S. (2013). Trace element partitioning between perovskite and kimberlite to carbonatite melt: New experimental constraints. *Chemical Geology* **353**, 132-139. https://doi.org/10.1016/j.chemgeo.2012.03.025.

Bizzaro, M. (2002). *Geochimie des Elements Majeurs et des Isotopes (Sr, Nd et Hf) de Peridotites Mantelliques, Carbonatites et Kimberlites du Canada et du Groenland; Implications pour la Dynamique du Manteau Terrestre.* Ph.D. Thesis, Universite du Quebec a Montreal.

Brett, R. C., Russell, J. K. & Moss, S. (2009). Origin of olivine in kimberlite: Phenocryst or impostor? *Lithos* **112**, 201-212. https:// doi.org/10.1016/j.lithos.2009.04.030.

Brey, G. P., Bulatov, V. K., Girnis, A. V. & Lahaye, Y. (2008). Experimental melting of carbonated peridotite at 6–10 GPa. *Journal of Petrology* **49**, 797 -821. https://doi.org/10.1093/petrology/egn002.

Bussweiler, Y., Foley, S.F., Prelevic, D., Jacob, D.E. (2015). The olivine macrocryst problem: New insights from minor and trace element compositions of olivine from Lac de Gras kimberlites, Canada. *Lithos* **220**, 238-252. http://dx.doi.org/10.1016/j.lithos.2015.02.016.

Canil, D. & Fedortchouk, Y. (1999). Garnet dissolution and the emplacement of kimberlites. *Earth and Planetary Science Letters* **167**, 227-237. https://doi.org/10.1016/S0012-821X(99)00019-9.

Chakhmouradian, A. R., Reguir, E. P. & Mitchell, R. H. (2002). Strontium-apatite: new occurrences, and the extent of Sr-for-Ca substitution in apatite-group minerals. *Canadian Mineralogist* **40**, 121-136.

Connelly, J. N., Thrane, K., Krawiec, A. W. & Garde, A. A. (2006). Linking the

1083 Palaeoproterozoic Nagssugtoqidian and Rinkian orogens through the Disko Bugt
1084 region of West Greenland. *Journal of the Geological Society* **163**, 319-335.
1085 https://doi.org/10.1144/0016-764904-115.

1086 Dalton, J. A. & Presnall, D. C. (1998a). Carbonatitic melts along the solidus of model
1087 lherzolite in the system CaO-MgO-Al_2O_3-SiO_2-CO_2 from 3 to 7 GPa.
1088 *Contributions to Mineralogy and Petrology* **131**, 123-135.
1089 https://doi.org/10.1007/s004100050383.

1090 Dalton, J. A. & Presnall, D. C. (1998b). The continuum of primary carbonatitic
1091 kimberlitic melt compositions in equilibrium with lherzolite: data from the
1092 system CaO-MgO-Al_2O_3-SiO_2-CO_2 at 6 GPa. *Journal of Petrology* **39,** 1953-
1093 1964. https://doi.org/10.1093/petroj/39.11-12.1953.

1094 Dalton, J. A. & Wood, B. J. (1993). The partitioning of Fe and Mg between olivine and
1095 carbonate and the stability of carbonate under mantle conditions.
1096 *Contributions toMineralogy and Petrology* **114**, 501-509.
1097 https://doi.org/10.1007/BF00321754.

1098 Dasgupta, R. & Hirschmann, M. M. (2007). Effect of variable carbonate concentration on
1099 the solidus of mantle peridotite. *American Mineralogist* **92**, 370-379.
1100 https://doi.org/10.2138/am.2007.2201.

1101 Dawson, J.B. (1971). Advances in kimberlite geology. *Earth-Science Reviews* **7**, 187-214.
1102 https://doi.org/10.1016/0012-8252(71)90120-6.

1103 Dawson & Hinton (2003). Trace-element content and partitioning in calcite, dolomite and
1104 apatite in carbonatite, Phalaborwa, South Africa. *Mineralogical Magazine*, **67**(5),
1105 921–930. https//doi.org/10.1180/0026461036750151.

1106 Enggist, A., Chu, L. & Luth, R. W. (2012). Phase relations of phlogopite with magnesite from
1107 4 to 8 GPa. *Contributions to Mineralogy and Petrology* **163**, 467-481. doi
1108 10.1007/s00410-011-0681-9.

1109 Exley, R. A. & Jones, A. P. (1983). $^{87}Sr/^{86}Sr$ in kimberlitic carbonates by ion microprobe:
1110 hydrothermal alteration, crustal contamination and relation to carbonatite.
1111 *Contributions to Mineralogy and Petrology* **83**, 288-292.

https://doi.org/10.1007/BF00371197.

Fedortchouk, Y. & Canil, D. (2004). Intensive variables in kimberlite magmas, Lac de Gras,Canada and implications for diamond survival. *Journal of Petrology* **45**, 1725- 1745. https://doi.org/10.1093/petrology/egh031.

Fleet, M. E. & Liu, X. (2007). Coupled substitution of type A and B carbonate in sodium-bearing apatite. *Biomaterials* **28**, 916-926. doi:10.1016/j.biomaterials.2006.11.003.

Foley, S. F. (1992). Vein-plus-wall-rock melting mechanisms in the lithosphere and the origin of potassic magmas. *Lithos* **28**, 435-453. https://doi.org/10.1016/0024-4937(92)90018-T.

Foley, S. F., Musselwhite, D. S. & Van der Lann, S. R. (1999). Melt compositions from ultramafic vein assemblages in the lithospheric mantle: a comparison of cratonic and non-cratonic settings. In: Gurney, J. J., Gurney, J. L., Pascoe, M. D. & Richardson, S. H. (ed.) *The J. B. Dawson Volume, Proceedings of the VIIth International Kimberlite Conference.* Cape Town: Red Roof Design, 574-583.

Foley, S. F., Yaxley, G. M. & Kjarsgaard, B. A. (2019). Kimberlites from source to surface: insights from experiments. *Elements* **15**, 393–398. https://doi.org/10.2138/gselements.15.6.393.

Foley, S. F., Yaxley, G. M., Rosenthal, A., Buhre, S., Kiseeva, E. S., Rapp, R. P. & Jacob, D. E. (2009). The composition of near-solidus melts of peridotite in the presence of CO_2 and H_2O between 40 and 60 kbar. *Lithos* **112S,** 274-283. https://doi.org/10.1016/j. lithos.2009.03.020.

Fraser, K. J. & Hawkesworth, C. J. (1992). The petrogenesis of group 2 ultrapotassic kimberlites from Finsch Mine, South Africa. *Lithos* **28,** 327-345. https://doi.org/10.1016/0024-4937(92)90013-O.

Garrit, D. (2000). *The nature of the Achaean and Proterozoic lithospheric mantle and lowercrust in West Greenland illustrated by the geochemistry and petrography of xenoliths from kimberlites*. Ph.D. Thesis, University of Copenhagen.

1140 Giuliani, A. (2018). Insights into kimberlite petrogenesis and mantle metasomatism from a
1141 review of the compositional zoning of olivine in kimberlites worldwide. *Lithos*
1142 **312**, 322-342. https://doi.org/10.1016/j.lithos.2018.04.029.

1143 Giuliani,A, Kamenetsky, V.S., Kendrick, M.A., Phillips, D, Wyatt, B.A. & Mass, R (2013).
1144 Oxide, sulphide and carbonate minerals in a mantle polymict breccia:
1145 metasomatism by proto-kimberlite magmas, and relationship to the kimberlite
1146 megacrystic suite. *Chemical Geology* **353**, 4–18.
1147 https://doi.org/10.1016/j.chemgeo.2012.09.025.

1148 Giuliani, A., Pearson, D.G., Soltys, A., Dalton, H.B., Phillips, D., Foley, S.F., Lim, E., Goemann, K.,
1149 Griffin, W.L., Mitchell, R.H. (2020). Kimberlite genesis from a common
1150 carbonate-rich primary melt modified by lithospheric mantle assimilation. *Science*
1151 *Advances* **6**, eaaz0424. DOI: 10.1126/sciadv.aaz0424.

1152 Giuliani, A., Phillips, D., Kamenetsky, V.S., Goemann, K. (2016). Constraints on
1153 kimberlite ascent mechanisms revealed by phlogopite compositions in
1154 kimberlites and mantle xenoliths. *Lithos* **240**, 189-201.
1155 http://dx.doi.org/10.1016/j.lithos.2015.11.013.

1156 Grunsky, E.C., Kjarsgaard, B.A. (2008). Classification of distinct eruptive phases of the
1157 diamondiferous Star kimberlite, Saskatchewan, Canada based on statistical
1158 treatment of whole rock geochemical analyses. *Applied Geochemistry* **23**, 3321-
1159 3336. doi:10.1016/j.apgeochem.2008.04.027.

1160 Gudfinnsson, G. H. & Presnall, D. C. (2005). Continuous gradations among primary
1161 carbonatitic, kimberlitic, melilititic, basaltic, picritic, and komatiitic melts in
1162 equilibrium with garnet lherzolite at 3–8 GPa. *Journal of Petrology* **46**, 1645 -
1163 1659. https://doi. org/10.1093/petrology/egi029.

1164 Hammouda, T., Chantel, J. & Devidal, J. (2010). Apatite solubility in carbonatitic liquids and
1165 trace element partitioning between apatite and carbonatite at high pressure.
1166 *Geochimica et Cosmochimica Acta* **74**, 7220-7235.
1167 https://doi.org/10.1016/j.gca.2010.09.032.

1168 Harmer, R. E. & Gittins, J. (1997). The origin of dolomitic carbonatites: field
1169 and experimental constraints. *Journal of African Earth Sciences* **25**,

5-28. https://doi.org/10.1016/S0899-5362(97)00059-6.

Jensen, S. M., Secher, K. & Rasmussen, T. M. (2004). Diamond content of three kimberlitic occurrences in southern West Greenland. Diamond identification results, field description and magnetic profiling. *Danmarks og Grønlands Geologiske Undersøgelse Rapport* **19,** 41 pp.

Jones, A. & Wyllie, P. J. (1984). Minor elements in perovskite from kimberlites and distribution of the rare earth elements: an electron probe study. *Earth and Planetary Science Letters* **69**, 128-140. https://doi.org/10.1016/0012-821X(84)90078-5.

Kamenetsky, V. S., Kamenetsky, M. Y., Sobolev, A. V., Golovin, V., Demouchy, S., Faure,K., Sharygin, V. V. & Kuzmin, D. V. (2008). Olivine in the Udachnaya-East Kimberlite (Yakutia, Russia): Types, Compositions and Origins. *Journal of Petrology* **49**, 823-839. https://doi.org/10.1093/petrology/egm033.

Kamenetsky, V. S., Kamenetsky, M. B., Weiss, Y., Navon, O., Nielsen, T. F. D. & Mernagh, T. P. (2009). How unique is the Udachnaya-East kimberlite? Comparison with kimberlites from the Slave Craton (Canada) and SW Greenland. *Lithos* **112** (Supplement 1), 334-346. https://doi.org/10.1016/j.lithos.2009.03.032.

Keppler, H. (2003). Water solubility in carbonatite melts. *American Mineralogist* **88**, 1822-1824. https://doi.org/10.2138/am-2003-11-1224.

Kjarsgaard, B. A., Pearson, D. G., Tappe, S., Nowell, G. M. & Dowall, D. P. (2009). Geochemistry of hypabyssal kimberlites from Lac de Gras, Canada: Comparisons to a global database and applications to the parent magma problem. *Lithos* **112S**, 236-248. https://doi.org/10.1016/j.lithos.2009.06.001.

Klemme, S. & Dalphé, C. (2003). Trace element partitioning between apatite and carbonatite melt. *American Mineralogist* **88**, 639-646.

Kushiro, I., Syono, Y. & Akimoto, S. (1967). Stability of phlogopite at high pressures and possible presence of phlogopite in the Earth's upper mantle. *Earth and Planetary Science Letters* **3**, 197-203. https://doi.org/10.1016/0012-821X(67)90036-2.

1199 Larsen, L.M. & Garrit, D. (2005). Mapping of the lithosphere beneath the Achaean craton
1200 and Proterozoic mobile belt in West Greenland. *Geological Survey of Denmark*
1201 *and Greenland Report* **68**, 55-56.

1202 Larsen, L. M. & Rex, D. C. (1992). A review of the 2500 Ma span of alkaline-ultramafic,
1203 potassic and carbonatitic magmatism in West Greenland. *Lithos* **28**, 367-402.
1204 https://doi.org/10.1016/0024-4937(92)90015-Q.

1205 le Roex, A.P. (1986). Geochemical correlation between southern African kimberlites and
1206 South Atlantic hotspots. *Nature* **324**, 243-245.
1207 https://doi.org/10.1038/324243a0.

1208 le Roex, A. P., Bell, D. R. & Davis, P. (2003). Petrogenesis of group I kimberlites from
1209 Kimberlite, South Africa: evidence from bulk-rock geochemistry. *Journal of*
1210 *Petrology* **44**, 2261-2286. https://doi. org/10.1093/petrology/egg077.

1211 Luth, R.W. (2009). The activity of silica in kimberlites, revisited. *Contributions to*
1212 *Mineralogy and Petrology* **158**, 283-294. https://doi. org/10.1007/s00410-
1213 009-0383-8.
1214 McDonough, W. F. & Sun, S.–s. (1995). The composition of the Earth. *Chemical Geology*
1215 **120**, 223-253. https://doi.org/10.1016/0009-2541(94)00140-4.

1216 McClennan, G. H. & Lehr, J. R. (1969). Crystal chemical investigation of natural apatites.
1217 *American Mineralogist* **54**, 1374-1391.

1218 McIntyre, T, Waterton, P., Vezinet, A., Szilas, K. & Pearson, D.G. (2021). Extent and age of
1219 Mesoarchean components in the Nagssugtoqidian orogen, West Greenland:
1220 Implications for tectonic environments and crust building in cratonic orogenic
1221 belts. Lithos, 396-397, 106182. https://doi.org/10.1016/j.lithos.2021.106182.

1222 Mitchell, R. H. (1986). *Kimberlites mineralogy, geochemistry, and petrology*. New
1223 York:Plenum Press, 442 pp.

1224 Mitchell, R. H. (1995). *Kimberlites, orangeites, and related rocks*. New York: Plenum Press,
1225 410 pp. https://doi.org/10.1007/978-1-4615-1993-5.

1226 Mitchell, R.H. (2008). Petrology of hypabyssal kimberlites: Relevance to primary magma
1227 compositions. *Journal of Volcanology and Geothermal Research* **174**, 1-8.
1228 doi:10.1016/j.jvolgeores.2007.12.024.

1229 Mitchell, R.H. (2013). Paragenesis and oxygen isotopic studies of serpentine in kimberlite. In:
1230 Pearson, D., *et al.* Proceedings of 10th International Kimberlite Conference.
1231 Springer, New Delhi. https://doi.org/10.1007/978-81-322-1170-9_1.

1232 Mitchell, R. H., Scott Smith, B. H. & Larsen, L. M. (1999). Mineralogy of ultramafic dikes
1233 from the Sarfartoq, Sisimuit and Maniitsoq areas, West Greenland. In: Gurney, J.
1234 J., Gurney, J. L., Pascoe, M. D. & Richardson, S. H. (ed.) *The P. H. Nixon*
1235 *Volume, Proceedings of the VIIth International Kimberlite Conference.* Cape
1236 Town: Red Roof Design, 574-583.

1237 Mitchell, R. H. & Tappe, S. (2010). Discussion of "Kimberlites and aillikites as probes of
1238 the continental lithospheric mantle", by D. Francis and M. Patterson (Lithos v.
1239 109, p. 72-80). *Lithos* **115**, 288-292. https://doi.org/10.1016/j.lithos.2009.10.017.

1240 Modreski, P. J. & Boettcher, A. L. (1973). Phase relationships of phlogopite in the system
1241 K_2O-MgO-CaO-Al_2O_3-SiO_2-H_2O to 35 kilobars: a better model for micas in the
1242 interior of the Earth. *American Journal of Science* **273**, 385-414.
1243 https://doi.org/10.2475/ajs.273.5.385.

1244 Moore, A., Yudovskaya, M., Proyer, A.& Blenkinsop, T. (2020). Evidence for olivine
1245 deformation in kimberlites and other mantle-derived magmas during crustal
1246 emplacement. *Contributions to Mineralogy and Petrology* **175**, 1–9.
1247 https://doi.org/10.1007/s00410-020-1653-8.

1248 Nielsen, T.F.D. & Jensen, S.M. (2005). The Majuagaaa calcite kimberlite dike, Maniitsoq,
1249 southern West Greenland. *Geological Survey of Denmark and Greenland Report*
1250 ***2005/43**, 71-75.*

1251 Nielsen, T. F. D. & Sand, K. K. (2008). The Majuagaa kimberlite dike, Maniitsoq region,
1252 West Greenland: constraints on an Mg-rich silicocarbonatitic melt composition
1253 from groundmass mineralogy and bulk compositions. *Canadian Mineralogist* **46**,
1254 1043-1061. https://doi.org/10.3749/canmin.46.4.1043.

1255 Nielsen, T. F. D., Jensen, S. M., Secher, K. & Sand, K. K. (2009). Distribution of
1256 kimberlite and aillikite in the Diamond Province of southern West Greenland: A
1257 regional perspective based on groundmass mineral chemistry and bulk
1258 compositions. *Lithos* **112S**, 358-371.
1259 https://doi.org/10.1016/j.lithos.2009.05.035.

1260 Nutman, A. P., Friend, C. R. L., Barker, S. L. L., McGregor, V. R. (2004). Inventory
1261 and assessment of Palaeoarchaean gneiss terrains and detrital zircons in
1262 southern West Greenland. *Precambrian Research* **135**, 281-314.
1263 doi:10.1016/j.precamres.2004.09.002.

1264 Otto, J. W. & Wyllie, P. J. (1993). Relationships between silicate melts and carbonate-
1265 precipitating melts in CaO-MgO-SiO_2-CO_2-H_2O at 2 kbar. *Mineralogy and*
1266 *Petrology* **48**, 343-365. https://doi.org/10.1007/BF01163107.

1267 Pan, Y. & Fleet, M. E. (2002). Compositions of the apatite-group minerals: substitution
1268 mechanisms and controlling factors. In: Kohn, M. J., Rakovan, J. & Hughe, J.
1269 M. (eds.) *Phosphates: Reviews in Mineralogy and Geochemistry* **48,** 13-49**.**
1270 Washington, D. C.: Mineralogical Society of America.
1271 https://doi.org/10.2138/rmg.2002.48.2.

1272 Pearce J. A. (2008). Geochemical fingerprinting of oceanic basalts with applications to
1273 ophiolite classification and the search for Archean oceanic crust. *Lithos* **100,**
1274 14-48. https://doi.org/10.1016/j.lithos.2007.06.016.

1275 Pearson, D.G., Woodhead, J., Janney, P.E. (2019). Kimberlites as geochemical probes
1276 of Earth's mantle. *Elements* **15**, 387-392.
1277 https://doi.org/10.2138/gselements.15.6.387.

1278 Pilbeam, L. Nielsen, T. F. D. & Waight, T. (2013). Digestion Fractional Crystallisation
1279 (DFC): an important process in the genesis of kimberlites. Evidence from olivine
1280 in the Majuagaa kimberlite, southern West Greenland. *Journal of Petrology* **54**
1281 (7), 1399–1425. https://doi.org/10.1093/petrology/egt016.

1282 Pilbeam, L., Rasmussen, T. M., Waight, T. & Nielsen, T. F. D. (2023). Inversion
1283 modelling of the kimberlite parental melt: an example from the Majuagaa dyke,
1284 southern West Greenland. *Journal of Petrology* **64**, 1–29.

DOI: 10.1093/petrology/egac127.

Price, S. E., Russell, J. K. & Kopylova, M. G. (2000). Primitive magma from the Jericho Pipe, N.W.T., Canada: Constraints on primary kimberlite melt chemistry. *Journal of Petrology* **41**, 789 -808. https://doi.org/10.1093/petrology/41.6.789.

Prowatke, S. & Klemme, S. (2006). Trace element partitioning between apatite and silicate melts. *Geochimica et Cosmochimica Acta* **70**, 4513-5427. https://doi.org/10.1016/j.gca.2006.06.162.

Reguir, E.P., Chakhmouradian, A.R., Halden, N.M., Malkovets, V.G., Yang, P. (2009). Major- and trace-element compositional variation of phlogopite from kimberlites and carbonatites as a petrogenetic indicator. *Lithos* **112**, 372-384. https://doi.org/10.1016/j.lithos.2009.05.023.

Ringwood, A. E., Kesson, S. E., Hibberson, W. & Ware, N. (1992). Origin of kimberlites and related magmas. *Earth and Planetary Science Letters* **113**, 521-538. https://doi.org/10.1016/0012-821X(92)90129-J.

Rooney, T.O., Girard, G., Tappe, S. (2020). The impact on mantle olivine resulting from carbonated silicate melt interaction. *Contributions to Mineralogy and Petrology* **175**,56, 1-15 pp. https://doi.org/10.1007/s00410-020-01694-0.

Russell, J.K., Jones, T.J. (2023). Transport and eruption of mantle xenoliths creates a lagging problem. *Commun Earth Environ* **4**, 177. https://doi.org/10.1038/s43247-023-00843-0.

Russell, J.K., Poritt, L.A., Lavallee, Y. & Dingwell, D.B. (2012). Kimberlite ascent by assimilation-fuelled buoyancy. *Nature* **481**, 352-357. Doi: 10.1038/nature10740.

Sand, K.K. (2007). *A geotherm for the cratonic lithospheric mantle in southern West Greenland: thermal implications for diamond potential*. MSc. thesis, University of Copenhagen, 126 pp.

Sand, K. K., Waight, T. E., Pearson, G., Nielsen, T. F. D., Makovicky, E. & Hutchison, M. T. (2009). The lithospheric mantle below southern West Greenland: a geothermobarometric approach to diamond potential and mantle stratigraphy.

Lithos **112** (Supplement 2), 1155–1166. doi: 0.1016/j.lithos.2009.05.012.

Sarkar, S., Giuliani, A., Dalton, H., Phillips, D., Ghosh, S., Misev, S. & Maas, R.((2023). Derivation of Lamproites and Kimberlites from a Common Evolving Source in the Convective Mantle: the Case for Southern African 'Transitional Kimberlites'. *Journal of Petrology* **64** (7), 16 pp. https://doi.org/10.1093/petrology/egad043.

Scott, B. H. (1977). *Petrogenesis of kimberlites and associated potassic lamprophyres from central West Greenland*. Ph.D. thesis, University of Edinburgh 340 pp.

Scott, B. H. (1981). Kimberlite and Lamproite dykes from Holsteinborg, West Greenland. *Meddelelser om Grønland, Geoscience* **4-1981,** 24 pp.

Secher K., Heaman, L. M., Nielsen, T. F. D., Jensen, S. M., Schjøth, F. & Creaser, R. A. (2009). Timing of kimberlite, carbonatite, and ultramafic lamprophyre emplacement in the alkaline province located 64º-67º N in southern West Greenland. *Lithos* **112** (Supplement 1), 400-406. doi:10.1016/j.lithos.2009.04.035.

Seifert, W., Kämpf, H. & Wasternack, J. (2000). Compositional variation in apatite, phlogopite and other accessory minerals of the ultramafic Delitzsch complex, Germany: implication for cooling history of carbonatites. *Lithos* **53**, 81–100. https://doi.org/10.1016/S0024-4937(00)00010-4.

Shaikh, A.M., Tappe, S., Bussweiler, Y., Vollmer, C., Brown, R.J. (2021). Origins of olivine in Earth's youngest kimberlite: Igwisi Hills volcanoes, Tanzania craton. *Contributions to Mineralogy and Petrology* **176**, 1-19. https://doi.org/10.1007/s00410-021-01816-2.

Shaw,D.M (1970). Trace element fractionation during anatexis. *Geochimica et Cosmochimica Acta* **34**, 237-243. 10.1016/0016-7037(70)90009-8.

Smith C.B., Haggerty, S.E., Chatterjee, B., Beard, A. & Townend, R. (2013). Kimberlite, lamproite, ultramafic lamprophyre, and carbonatite relationships on the Dharwar Craton, India; an example from the Khaderpet pipe, a diamondiferous ultramafic with associated carbonatite intrusion. *Lithos* **182–183**, 102-113. https://doi.org/10.1016/j.lithos.2013.10.006.

1343 Soltys, A., Giuliani, A. & Phillips, D. (2018). A new approach to reconstructing the
1344 composition and evolution of kimberlite melts: a case study of the archetypal
1345 Bultfontein kimberlite (Kimberley, South Africa). *Lithos* **304–307**, 1–15 .
1346 10.1016/j.lithos.2018.01.027.

1347 Soltys, A., Giuliani, A. & Phillips, D. (2020b). Apatite compositions and groundmass
1348 mineralogy record divergent melt/fluid evolution trajectories in coherent
1349 kimberlites caused by differing emplacement mechanisms. *Contributions to*
1350 *Mineralogy and Petrology* **175**:49, 31 pp. https://doi.org/10.1007/s00410-020-
1351 01686-0.

1352 Soltys, A., Giuliani, A., Phillips, D. & Kamenetsky, V. S. (2020a). Kimberlite metasomatism of the
1353 lithosphere and the evolution of olivine in carbonate-rich melts — evidence from the
1354 Kimberley kimberlites (South Africa). Journal of Petrology **61**. 31 pp.
1355 https://doi.org/10.1093/petrology/egaa062.

1356 Sparks, R. S. J., Brooker, R. A., Field, M., Kavanagh, J., Schumacher, J. C., Walter, M. J. &
1357 White, J. (2009). The nature of erupting kimberlitic melts. *Lithos* **112S**, 429-438.
1358 10.1016/j.lithos.2009.05.032.

1359 Tainton, K.M. & McKenzie, D. (1994). The generation of kimberlites, lamproites and
1360 their source rocks. *Journal of Petrology* **35**, 787-817.
1361 https://doi.org/10.1093/petrology/35.3.787.

1362 Tappe, S., Brand, N.B., Stracke, A., van Acken, D., Liu, C.-Z., Strauss, H., Wu, F.-Y., Luguet,
1363 A., Mitchell, R.H. (2017a). Plates or plumes in the origin of kimberlites: U/Pb
1364 perovskite and Sr-Nd-Hf-Os-C-O isotope constraints from the Superior craton
1365 (Canada). *Chemical Geology* **455**, 57-83.
1366 https://doi.org/10.1016/j.chemgeo.2016.08.019.

1367 Tappe, S., Foley, S. F., Jenner, G. A., Heaman, L. M., Kjarsgaard, B. A., Romer, R. L.,
1368 Stracke, A., Joyce, N. & Hoefs, J. (2006). Genesis of ultramafic lamprophyres
1369 and carbonatites at Aillik Bay, Labrador: a consequence of incipient
1370 lithospheric thinning beneath the North Atlantic Craton. *Journal of Petrology*
1371 **47**, 1261-1315. https://doi.org/10.1093/petrology/egl008.

1372 Tappe, S., Foley, S. F., Jenner, G. A. & Kjarsgaard, B. A. (2005). Integrating

ultramafic lamprophyres into the IUGS classification of igneous rocks: rationale and implications. *Journal of Petrology* **46**, 1893-1900. https://doi.org/10.1093/petrology/egi039.

Tappe, S., Foley, S. F., Kjarsgaard, B. A., Romer, R. L., Heaman, L. M., Stracke, A. & Jenner, G. A. (2008). Between carbonatite and lamproites – Diamondiferous Torngat ultramafic lamprophyres formed by carbonate-fluxed melting of cratonic MARID-type metasomes. *Geochimica et Cosmochimica Acta* **72**, 3258-3286. https://doi.org/10.1016/j.gca.2008.03.008.

Tappe, S., Jenner, G. A., Foley, S. F., Heaman, L., Besserer, D., Kjarsgaard, B. A. & Ryan, B. (2004). Torngat ultramafic lamprophyres and their relation to the North Atlantic Alkaline Province. *Lithos* **76**, 491-518. https://doi.org/10.1016/j.lithos.2004.03.040.

Tappe, S., Kjarsgaard, B.A., Kurszlaukis, S., Nowell, G.M., Phillips, D. (2014). Petrology and Nd-Hf isotope geochemistry of the Neoproterozoic Amon kimberlite sills, Baffin Island (Canada): Evidence for deep mantle magmatic activity linked to supercontinent cycles. *Journal of Petrology* **55**, 2003-2042. https://doi.org/10.1016/j.lithos.2004.03.040.

Tappe, S., Pearson, D.G., Nowell, G., Nielsen, T.F.D., Milstead, P. & Muehlenbachs, K. (2011a). A fresh isotopic look at Greenland kimberlites: Cratonic mantle lithosphere imprint on deep source signal. *Earth and Planetary Science Letters* **305,** 235-248. https://doi. org/10.1016/j.epsl.2011.03.005.

Tappe, S., Romer, R.L., Stracke, A., Steenfelt, A., Smart, K.A., Muehlenbachs, K., Torsvik, T.H. (2017b). Sources and mobility of carbonate melts beneath cratons, with implications for deep carbon cycling, metasomatism and rift initiation. *Earth and Planetary Science Letters* **466**, 152-167. https://doi.org/10.1016/j.epsl.2017.03.011.

Tappe, S., Smart, K.A., Pearson, D.G., Steenfelt, A., Simonetti, A. (2011b). Craton formation in Late Archean subduction zones revealed by first Greenland eclogites. *Geology* **39**, 1103-1106. https://doi.org/10.1130/G32348.1.

1402 Tappe, S., Smart, K.A., Torsvik, T.H., Massuyeau, M., de Wit, M.C.J. (2018). Geodynamics
1403 of kimberlites on a cooling Earth: Clues to plate tectonic evolution and deep
1404 volatile cycles. *Earth and Planetary Science Letters* **484**, 1-14.
1405 https://doi.org/10.1016/j.epsl.2017.12.013.

1406 Tappe, S., Steenfelt, A., Heaman, L.M., Simonetti, A. (2009). The newly discovered Jurassic
1407 Tikiusaaq carbonatite-aillikite occurrence, West Greenland, and some remarks on
1408 carbonatite-kimberlite relationships. *Lithos* **112**, 385-399.
1409 https://doi.org/10.1016/j.lithos.2009.03.002.

1410 Tappe, S., Steenfelt, A. & Nielsen, T. F. D. (2012). Asthenospheric source of Neoproterozoic
1411 and Mesozoic kimberlites from the North Atlantic Craton, West Greenland: new
1412 high-precision U-Pb and Sr-Nd isotope data on perovskite. Chemical Geology
1413 320-321, 113–127. https://doi.org/10.1016/j.chemgeo.2012.05.026.

1414 Ulmer, P. & Sweeney, R. J. (2002). Generation and differentiation of Group II
1415 kimberlites:Constraints from a high-pressure experimental study to 10GPa.
1416 *Geochimica et Cosmochimica Acta* **66**, 2139-2153.
1417 https://doi.org/10.1016/S0016-7037(02)00898-0.

1418 Veksler, I. V. & Keppler, H. (2000). Partitioning of Mg, Ca and Na between carbonatite
1419 melt and hydrous fluid at 0.1-0.2 GPa. *Contributions to Mineralogy and*
1420 *Petrology* **138**, 27-34. https://doi.org/10.1007/PL00007659.

1421 Wang, C., Zhang, Z., Giuliani, A, Cheng,Z., Liu, B. & Kong, W. (2021). Geochemical
1422 and O–C–Sr–Nd Isotopic Constraints on the Petrogenetic Link between
1423 Aillikites and Carbonatites in the Tarim Large Igneous Province, *Journal of*
1424 *Petrology* **62** (5), 1-21. https://doi.org/10.1093/petrology/egab017.

1425 Windley, B. F., Garde, A. A. (2009). Arc-generated blocks with crustal sections in the
1426 North Atlantic craton of West Greenland: crustal growth in the Archean with
1427 modern analogues. *Earth-Science Reviews* **93**, 1-30.
1428 https://doi.org/10.1016/j.earscirev.2008.12.001.

1429 Wittig, N., Pearson, D. G., Webb, M., Ottley, C. J., Irvine, G. J., Kopylova, M., Jensen, S.
1430 M.& Nowell, G. M. (2008). Origin of cratonic lithospheric mantle roots: A
1431 geochemical study of peridotites from the North Atlantic Craton, West

Greenland. *Earth and Planetary Science Letters* **274**, 24-33. https://doi.org/10.1016/j.epsl.2008.06.034.

Wittig, N., Webb, M., Pearson, D. G., Dale, C. W., Ottley, C. J., Hutchinson, M., Jensen, S. M. & Luguet, A. (2010). Formation of the North Atlantic Craton: Timing and mechanisms constrained from Re-Os isotope and PGE data of peridotite xenoliths from S.W. Greenland. *Chemical Geology* **276**, 166-187. https://doi.org/10.1016/j.epsl.2008.06.034.

Yaxley, G.M., Anenburg, M., Tappe, S., Decree, S., Guzmics, T. (2022). Carbonatites: classification, sources, evolution, and emplacement. *Annual Review of Earth and Planetary Sciences* **50**, 261-293. https://doi.org/10.1146/annurev-earth-032320-104243.

Yoder, H. S. Jr. & Kushiro, I. (1969). Melting of a hydrous phase: phlogopite. *American Journal of Science* **267-A**, 558-582.

TABLES

Table 1: Representative electron microprobe (EMP) data for clinopyroxene in the Maniitsorsuaq mela-aillikite and Sarfartuup Nuna South aillikite.

Table 2: Representative EMP data for apatite in the four occurrences.

Table 3: Representative EMP data for perovskite.

Table 4: EMP data for calcite in Majuagaa (kimberlite *s.s.*), Sarfartuup Nuna South (aillikite) and Maniitsorsuaq (mela-aillikite).

Table 5: New bulk rock geochemical data by XRF and ICP-MS. Table 5a: Maniitsorsuaq and Table 5b: P-dyke and Sarfartuup Nunat South. Analytical methods are found in supplementary information SI1, full data set in SI9.

Table 6: Estimation of the proportions of the contributions of three theoretical end-members

1458 to the bulk rock compositions

FIGURE CAPTIONS

Fig. 1: Southern West Greenland with kimberlite and aillikite provinces and the locations of the four occurrences included in this study. Majuagaa (calcite kimberlite), P-Dyke (transitional between kimberlite and aillikite), Sarfartuup Nuna South (aillikite), and Maniitsorsuaq (mela-aillikite).

Fig.2: Field scale textures in the kimberlites and ultramafic lamprophyres. (Scale from: hammer ~50x3cm, notebook ~ 15x8cm.) (a) central xenolith accumulation and foliation near contacts in Maniitsorsuaq. (b) flow foliation and flow alignment of xenoliths in Maniitsorsuaq. (c) flow foliation at margins and massive textured centre of outcrop from Maniitsorsuaq. (d) lateral flow foliation in a rotated block of the Majuagaa calcite kimberlite dyke (reproduced with permission from GEUS).

Fig. 3: Backscattered electron images of textures in the Majuagaa kimberlite, the Sarfartuup Nuna South aillikite and the Maniitsorsuaq mela-aillikite. (a) accumulation of euhedral apatite 1 (lightest shade) in apatite 2 in the matrix of the Majuagaaa kimberlite. The rest of the image is calcite (lighter) and dolomite (darker). Dolomite is interstitial to calcite. Note the blebby exsolution of dolomite from calcite. The white lines are 20μm apart; (b) Potential calcite microphenocrysts (lighter) in a matrix of dolomite (darker) in the groundmass of the Majuagaa kimberlite. Note the blebby exsolution of both calcite from dolomite and dolomite from calcite; (c) Perovskite overgrowth and enclosure of apatite and phlogopite; (d) replacement of calcite by serpentine in Maniitsorsuaq (white lines 20μm apart); (e) phlogopite grain with disequilibrium core in Jesper blow of Sarfartuup Nuna.South aillikite. Note the characteristic replacement of calcite by serpentine; (f) rare ilmenite macrocryst in the Maniitsorsuaq mela-aillikite. Note the extensive overgrowth by spinel and perovskite; and (g) phlogopite grains in the groundmass of Maniitsorsuaq mela-aillikite.

Fig. 4: Crystallization sequences of kimberlite versus aillikite/mela-aillikite, as deduced from the petrographic relations between the phases.

Fig. 5: All electron microprobe analyses for Ni and Fo% in olivine in the Sarfartuup Nuna South aillikite (a) and Maniitsorsuaq mela-aillikite (b). (c) un-zoned grains in the groundmass of Sarfartuup Nunat South aillikite. The blue field in (c): cognate margins (from panel (a). Data in SI2 in supplementary information. The two black-lined polygons represent the compositional fields for olivine in mantle xenoliths (Sand, 2007) and olivine in ilmenite dunite xenoliths (Bizzarro, 2002). Legend in panel (a).

Fig. 6: Fo vs Ni transects across representative types of macrocryst grains. The spacing between point analyses is 5µm. (a-d) transects from Sarfartuup Nuna South aillikite and (e-f) from Maniitsorsuaq mela-aillikite. Dark zones (d) identified in figures 6c and d.

Fig. 7: Regional phlogopite dataset (SI5) and from Nielsen *et al*. (2009). Legend in figure.

Fig. 8: EMPA data for apatite (Table 2 and SI6) recalculated to atoms per formula units on a 25oxygen basis. Plot (a) Na vs. total measured elements at the phosphorus site, this suggests the presence of an unmeasured and correlated element at the phosphorus site in the Majuagaa kimberlite. Plot (b) Si substitution for phosphorus is present in at all but the calcite-kimberlite; (c) La and Ce (ppm). Three analyses of apatite in Majuagaa calcite-kimberlite with higher La and Ce concentration are beyond the limits of the diagram.

Fig.9: Selected major element plots against MgO (SI9) for samples from the Maniitsorsuaq mela-aillikite. Solid arrows represent the qualitative effect of adding various mineral phases to the averaged bulk rock concentrations. Arrows show the qualitative effect of adding identified phases (averages of EMPA analyses) to the averaged bulk rock concentrations; Ol: olivine (cores and margins), Cpx: clinopyroxene, Phl: phlogopite (this work and Nielsen *et al*., 2009), Spn: groundmass spinel (Nielsen *et al.*, 2009), and Cc: calcite. Arrows for Rb and Sc are

1508 constrained by element partitioning constraints. Analyses of high-serpentine samples are
1509 circled.

1510 Fig. 10: Selected major element variations between samples from the Sarfartuup Nuna South
1511 aillikite (SI9). Arrows show the qualitative effect of adding identified phases (averages of
1512 EMPA analyses) to the averaged bulk rock concentrations; Ol: olivine (cores and margins),
1513 Cpx: clinopyroxene, Phl: phlogopite (this work and Nielsen *et al*., 2009), Spn: groundmass
1514 spinel (Nielsen *et al.*, 2009), and Cc: calcite. Arrows for Rb and Sc are constrained by element
1515 partitioning constraints.

1516 Fig. 11: Major element compositions in the calcite-kimberlites, aillikites and mela-aillikites
1517 of southern West Greenland and Labrador. Literature analyses of kimberlites *s.l.* in S.W.
1518 Greenland: Nielsen & Sand (2008), Nielsen *et al*. (2009) and Tappe *et al*. (2011a), and from
1519 northern Labrador: Tappe *et al*. (2004; 2008). The black rosettes illustrate the effects on bulk
1520 rock compositions of addition of the indicated minerals and of degassing . Ol –olivine, Cpx –
1521 clinopyroxene, Phl – phlogopite, Spn – spinel, Ilm – ilmenite, Cc – calcite, and Srp-
1522 serpentine (see text).

1523 Fig. 12: Variation of Ni and MgO in the calcite-kimberlites, aillikites and mela-aillikites of
1524 S.W. Greenland and Labrador. The variation is broadly controlled by olivine. The trend
1525 defined by the Majuagaa dyke is controlled by dissolution of orthopyroxene (see text). New
1526 data in table SI9 and previously published data from Nielsen and Sand (2008), Nielsen *et al*.
1527 (2009), Tappe *et al*. (2004, 2008 and 2011a) and GEUS data base.

1528 Fig. 13: Constraints for the major element melt compositions of the kimberlites, aillikites and
1529 mela-aillikites of S.W. Greenland and Labrador. Variations in MgO are largely due to
1530 entrained lithospheric material and ratios between elements and MgO are proxies for melt
1531 composition (see text for explanation).

Fig. 15*:* Variation in compatible elements in melts of kimberlites, aillikites and mela-aillikites. See text and Fig. 13 for rational for using ratio over MgO as proxy for melt composition. Note the tight clustering for Majuagaa calcite-kimberlite versus the noticeable trend in proxy-melt compositions for the Maniitsorsuaq mela-aillikite. The transitional P-dyke and the aillikite from Sarfartuup Nuna South are transitional between calcite-kimberlite and mela-aillikite.

Fig. 15: Multi-element plot of incompatible trace elements normalized to primitive mantle (McDonough & Sun, 1995) following Tappe *et al*. (2011). Thin colored lines are analyses for individual samples in this study: Majuagaa kimberlite data from Nielsen & Sand (2008) and Labrador data after Tappe *et al*. (2004; 2008).

Fig. 16: Incompatible element variations in melts using element/MgO as proxy for melt composition (see text for details). Differences in REE at same SiO_2/MgO between Majuagaa calcite-kimberlite and the P-dyke reflect variations in apatite proportion (Fig. 3a) and the Sarfartuup Nuna South and Maniitsorsuaq mela-aillikites show negative correlation between REE and SiO_2 reflecting dilution by a comparatively less REE-rich and more SiO_2-rich melt component.

Fig. 17: Modeling of the bulk rock compositions of the four occurrences as the result of a three-component mixing. HARZ: ilmenite- harzburgite assimilate (Pilbeam *et al*., 2023); PKM: modelled primary melt for the Majuagaa dyke (Pilbeam *et al*., 2023), and LM: experimental melt of phlogopite-clinopyroxene veins (Foley *et al*., 1999). The ellipses on end-members are the estimated confidence intervals. The lines drawn at 20% mixing intervals. HARZ and LM are coincident in panel (f).

Table 1. Representative EMP analyses of clinopyroxene (full data set in supplementary information)*

	Maniitsorsuaq (mela-ailikite)						Sarfartuup Nuna S (aillikite s.s.)					
Sample	513595	513595	517907	517907	517910	517910	491924	491924	491908	491908	491924	491924
Analysis (wt.%)												
SiO_2	45.50	44.40	50.80	50.60	46.80	47.00	52.50	53.20	50.70	51.00	50.60	50.70
TiO_2	3.24	3.26	1.88	1.63	3.51	2.36	1.15	0.80	1.23	1.11	1.94	1.75
Al_2O_3	6.57	6.00	2.43	2.57	6.18	4.14	1.27	0.88	2.34	2.67	1.05	0.99
Cr_2O_3	*n.d.*	0.06	0.04	0.02	0.02	0.03	n.d.	0.05	*n.d.*	*n.d.*	0.02	0.03
FeO_T	7.75	7.69	5.54	6.28	6.87	6.07	4.65	3.41	5.37	5.17	6.59	6.26
NiO	0.00	0.03	0.00	0.05	0.04	0.02	0.03	0.02	0.01	0.02	0.00	0.01
MnO	0.15	0.15	0.30	0.23	0.04	0.06	0.05	0.03	0.10	0.14	0.32	0.28
MgO	12.92	12.81	14.74	14.53	13.17	13.88	15.77	16.37	14.84	14.94	13.50	13.77
CaO	24.08	23.29	24.95	24.93	24.83	25.03	25.19	25.52	24.76	24.89	23.06	23.32
BaO	n.d.	0.05	0.06	n.d.	0.06	n.d.	-	-	-	-	-	-
Na_2O	0.29	0.32	0.26	0.28	0.33	0.28	0.25	0.24	0.34	0.35	1.03	0.88
K_2O	0.01	0.15	0.01	*n.d.*	0.02	0.03	*n.d.*	0.01	0.02	0.03	0.01	0.00
Total	100.51	98.17	100.98	101.07	101.87	98.88	100.86	100.51	99.72	100.34	98.12	98.03
Cations from calculation based on 6 oxygen to 4 cations												
Si	1.69	1.68	1.86	1.85	1.71	1.76	1.91	1.93	1.87	1.87	1.91	1.92
Ti	0.09	0.09	0.05	0.04	0.1	0.07	0.03	0.02	0.03	0.03	0.06	0.05
Al	0.29	0.27	0.1	0.11	0.27	0.18	0.05	0.04	0.1	0.12	0.05	0.04
Cr	n.d.	n.d.	*n.d.*	*n.d.*	*n.d.*	*n.d.*	*n.d.*	*n.d.*	*n.d.*	*n.d.*	*n.d.*	*n.d.*
Fe_T	0.24	0.24	0.17	0.19	0.21	0.19	0.14	0.1	0.17	0.16	0.21	0.2
Ni	*n.d.*	*n.d.*	*n.d.*	*n.d.*	*n.d.*	*n.d.*	*n.d.*	*n.d.*	*n.d.*	*n.d.*	*n.d.*	*n.d.*
Mn	*n.d.*	*n.d.*	0.01	0.01	*n.d.*	*n.d.*	*n.d.*	*n.d.*	*n.d.*	*n.d.*	0.01	0.01
Mg	0.71	0.72	0.8	0.79	0.72	0.77	0.86	0.89	0.82	0.82	0.76	0.77
Ca	0.96	0.95	0.98	0.98	0.97	1.00	0.98	0.99	0.98	0.98	0.93	0.94
Ba	*n.d.*	*n.d.*	*n.d.*	*n.d.*	*n.d.*	*n.d.*	-	-	-	-	-	-
Na	0.02	0.02	0.02	0.02	0.02	0.02	0.02	0.02	0.02	0.02	0.08	0.06
K	*n.d.*	*0.01*	*n.d.*	*n.d.*	*n.d.*	*n.d.*	*n.d.*	*n.d.*	*n.d.*	*n.d.*	*n.d.*	*n.d.*
Fe^{3+}	0.06	0.07	0.03	0.04	0.05	0.06	0.02	0.02	0.04	0.04	0.03	0.03
Fe^{2+}	0.18	0.18	0.14	0.15	0.16	0.13	0.12	0.08	0.13	0.12	0.18	0.17
FeO (wt.%)	5.8	5.6	4.5	5	5.2	4.1	3.8	2.7	4.2	4	5.7	5.4
Fe_2O_3 (wt.%)	2.1	2.5	1.1	1.4	1.7	2.3	0.9	0.8	1.3	1.3	1.2	1.1

Table 2: Representative EMP data for apatite (full dataset in supplementary information)

	Majuagaa (kimberlite *s.s.*)					P-Dyke (tUML)			Sarfartuup Nuna (S) (aillikite *s.s.*)					Maniitsorsuaq (mela-aillikite)				
Sample	491702	491702	491712	491745	491745	513507	513507	513507	513514	513536	513537	513537	513537	517910	517910	517910	517910	517910
Analysis (wt.%)																		
CaO	52.70	53.90	54.50	49.00	53.00	56.00	55.70	55.40	55.60	54.30	55.40	55.00	55.70	55.60	54.80	54.70	55.40	54.80
SrO	0.39	0.22	0.25	1.07	0.33	0.42	0.45	0.33	0.53	0.34	0.33	0.37	0.36	0.84	0.64	0.90	0.67	0.66
Na_2O	1.48	1.04	0.48	3.39	1.22	0.08	0.10	0.15	0.11	0.24	0.11	0.05	0.15	0.07	0.08	0.09	0.03	0.23
La_2O_3	0.14	0.05	0.16	0.17	0.07	*n.d.*	0.02	0.03	*n.d.*	0.04	*n.d.*	0.08	*n.d.*	*n.d.*	0.05	0.05	*n.d.*	*n.d.*
Ce_2O_3	0.24	0.17	0.30	0.50	0.28	*n.d.*	0.17	0.14	0.01	*n.d.*	0.06	0.04	0.11	*n.d.*	*n.d.*	0.01	0.06	*n.d.*
Sm_2O_3	-	-	-	0.04	*n.d.*	*n.d.*	*n.d.*	0.12	*n.d.*	0.07	0.09	0.04	0.07	-	-	-	-	-
P_2O_5	36.6	37.5	40.3	33.0	39.4	36.9	36.7	37.2	39.5	36.6	38.0	40.0	36.8	40.1	35.6	36.7	36.8	38.7
SiO_2	0.17	0.17	0.59	0.02	0.01	2.20	2.45	2.27	1.24	2.87	2.10	1.19	2.68	1.13	2.37	1.92	1.69	0.61
F*	3.4	3.6	3.9	3.1	3.7	3.4	3.4	3.5	3.9	3.6	3.7	3.9	3.8	1.8	1.7	2.1	1.8	2.7
Cl	*n.d.*	*n.d.*	*n.d.*	*n.d.*	*n.d.*	*n.d.*	*n.d.*	*n.d.*	*n.d.*	0.1	*n.d.*	0.1	*n.d.*	*n.d.*	*n.d.*	*n.d.*	*n.d.*	*n.d.*
Total	95.1	96.5	100.4	90.3	98.1	99.1	98.9	99.2	100.9	98.1	99.8	100.7	99.6	99.5	95.2	96.5	96.5	97.6
La (µg/g)	1202	443	1330	1458	571	*n.d.*	162	230	*n.d.*	341	*n.d.*	657	*n.d.*	*n.d.*	435	409	*n.d.*	*n.d.*
Ce (µg/g)	2032	1451	2561	4260	2391	*n.d.*	1434	1153	120	*n.d.*	495	299	939	*n.d.*	*n.d.*	77	487	*n.d.*
Sm (µg/g)	-	-	-	336	*n.d.*	*n.d.*	*n.d.*	1000	*n.d.*	578	776	379	569	-	-	-	-	-
Cations from recalculation on 25 oxygen basis																		
Ca	10.39	10.44	10.10	10.37	10.01	10.84	10.83	10.71	10.38	10.68	10.58	10.24	10.81	10.27	10.91	10.70	10.76	10.39
Sr	0.04	0.02	0.03	0.12	0.03	0.04	0.05	0.03	0.05	0.04	0.03	0.04	0.04	0.08	0.07	0.10	0.07	0.07
Na	0.53	0.36	0.16	1.30	0.42	0.03	0.03	0.05	0.04	0.08	0.04	0.02	0.05	0.02	0.03	0.03	0.01	0.08
La	0.01	0.00	0.01	0.01	*n.d.*	*n.d.*	*n.d.*	*n.d.*	*n.d.*	*n.d.*	*n.d.*	*n.d.*	*n.d.*	*n.d.*	*n.d.*	*n.d.*	*n.d.*	*n.d.*
Ce	0.02	0.01	0.02	0.04	0.02	*n.d.*	0.01	0.01	*n.d.*	*n.d.*	*n.d.*	*n.d.*	0.01	*n.d.*	*n.d.*	*n.d.*	*n.d.*	*n.d.*
Sm	-	-	-	*n.d.*	*n.d.*	*n.d.*	*n.d.*	0.01	*n.d.*	*n.d.*	0.01	*n.d.*	*n.d.*	-	-	-	-	-
P	5.71	5.73	5.90	5.51	5.88	5.64	5.63	5.68	5.82	5.69	5.74	5.88	5.64	5.86	5.60	5.67	5.66	5.80
Si	0.03	0.03	0.10	*n.d.*	*n.d.*	0.40	0.44	0.41	0.22	0.53	0.37	0.21	0.49	0.19	0.44	0.35	0.31	0.11
Cation sum	16.69	16.57	16.21	17.35	16.37	16.55	16.56	16.49	16.29	16.50	16.41	16.18	16.56	16.23	16.61	16.50	16.51	16.34
F	0.94	0.97	1.01	0.93	0.99	0.94	0.92	0.95	1.03	0.99	0.99	1.02	1.04	0.48	0.47	0.58	0.50	0.71
Cl	*n.d.*	*n.d.*	*n.d.*	*n.d.*	*n.d.*	*n.d.*	*n.d.*	*n.d.*	*n.d.*	*n.d.*	*n.d.*	*n.d.*	*n.d.*	*n.d.*	*n.d.*	*n.d.*	*n.d.*	*n.d.*
OH	0.06	0.03	0.00	0.07	0.01	0.06	0.08	0.05	*n.d.*	0.01	0.01	*n.d.*	*n.d.*	0.52	0.53	0.42	0.50	0.29
∑Ca site	10.98	10.84	10.31	11.84	10.49	10.91	10.92	10.81	10.47	10.80	10.67	10.30	10.92	10.37	11.02	10.83	10.85	10.54
∑P site	5.74	5.76	6.00	5.52	5.89	6.04	6.08	6.09	6.04	6.22	6.11	6.09	6.13	6.05	6.04	6.02	5.97	5.91

- Fluor in apatite estimated using standard set up (15nA, 15kV, TAPH, 20s count time). Fifty analyses of Wilberforce apatite gave an average of 4.07 +/- 0.28 wt.% F and a reproducibility of ca. 7%.

Table 3: Representative EMP data for perovskite (full dataset in supplementary information)

	Majuagaa		P-Dyke		Sarfartuup Nuna (S)		Maniitsorsuaq	
Sample	491725	491702	513507	513507	513536	513537	517910	517905
Analysis (wt%)								
SiO_2	0.46	*n.d.*	*n.d.*	*n.d.*	*n.d.*	*n.d.*	0.04	*n.d.*
TiO_2	50.1	56.7	55.9	56.2	57.7	58.4	57.6	56.3
Al_2O_3	0.33	0.29	0.46	0.47	0.3	0.26	0.13	0.18
Fe_2O_3	1.89	0.85	1.58	1.61	1.22	1.28	1.08	1.20
CaO	34.4	38.6	39.2	39.5	40.0	39.8	39.9	39.3
SrO	0.14	0.10	0.13	0.13	0.14	0.13	0.17	0.11
Na_2O	0.89	0.47	0.29	0.34	0.22	0.20	0.31	0.35
La_2O_3	1.16	0.67	0.51	0.50	0.18	0.23	0.18	0.12
Ce_2O_3	3.44	1.88	1.68	1.81	0.72	0.73	1.11	0.91
Sm_2O_3	-	-	0.12	0.06	*n.d.*	*n.d.*	-	-
Nb_2O_5	4.75	1.18	0.43	0.60	0.25	0.32	0.28	0.32
Total	97.34	100.57	100.22	101.15	100.77	101.35	100.61	98.66
La (µg/g)	9883	5679	4384	4265	1543	1995	1535	989
Ce (µg/g)	29370	16051	14343	15453	6173	6215	9451	7778
Sm (µg/g)	-	-	1007	511	*n.d.*	*n.d.*	-	-
Nb (µg/g)	33205	8235	3039	4186	1727	2216	1943	2251

Table 4: EMP data for calcite (full data set in supplementary information)

	Majuagaa (calcite-kimberlite *s.s.*)									Sarfartuup Nuna (S) (aillikite *s.s.*)								
Sample	491725	491725	491725	491725	491725	491725	491725	491725	491725	513535	513535	513535	513535	513535	513535	513535	513535	513535
Analysis (wt.%)																		
SiO_2	*n.d.*	*n.d.*	*n.d.*	*n.d.*	*n.d.*	0.1	*n.d.*	*n.d.*	*n.d.*	0.1	0.1	*n.d.*	*n.d.*	*n.d.*	*n.d.*	*n.d.*	*n.d.*	*n.d.*
FeO_T	0.17	0.32	0.90	0.50	0.21	0.77	0.09	0.16	0.45	0.41	0.59	0.52	0.35	0.19	0.86	0.22	0.17	0.28
MnO	0.05	*n.d.*	0.15	0.08	*n.d.*	*n.d.*	*n.d.*	0.01	0.35	0.03	0.47	0.09	0.52	0.26	0.03	0.26	0.24	*n.d.*
MgO	0.57	0.18	0.11	0.12	0.22	0.38	0.16	0.07	0.19	0.25	0.30	0.44	0.32	0.22	0.66	0.24	0.37	0.14
CaO	54.8	56.2	56.7	55.5	55.4	55.9	56.0	56.2	55.0	55.0	54.1	53.8	55.3	54.9	52.4	55.3	55.5	55.4
SrO	0.39	0.37	0.06	0.10	0.11	0.15	0.17	0.08	0.15	0.57	0.47	0.79	0.34	0.21	0.61	0.59	0.44	0.64
BaO	0.04	0.15	0.08	0.09	0.06	0.01	0.11	*n.d.*	*n.d.*	0.14	0.06	*n.d.*	*n.d.*	0.05	0.02	0.07	*n.d.*	0.01
Na_2O	0.04	0.13	0.04	0.06	0.01	0.06	0.04	0.07	0.07	*n.d.*	0.03	0.06	*n.d.*	*n.d.*	0.07	0.05	0.04	*n.d.*
CO_2	43.0	44.1	44.5	43.6	43.5	43.9	44.0	44.1	43.2	43.1	42.4	42.2	43.4	43.1	41.1	43.4	43.5	43.5
Total	99.09	101.48	102.55	100.01	99.55	101.28	100.58	100.63	99.39	99.59	98.57	97.86	100.14	98.97	95.75	100.04	100.23	99.91

Table 4 cont..: EMP data for calcite (full data set in suppl. information)

	Maniitsorsuaq (mela-aillikite)									
Sample	517910	517910	517910	517910	517910	517910	517910	517910	517910	517910
Analysis (wt%)										
SiO_2	*n.d.*	*n.d.*	*n.d.*	*n.d.*	*n.d.*	*n.d.*	*n.d.*	*n.d.*	*n.d.*	*n.d.*
FeO_T	0.02	0.19	0.03	0.19	0.29	0.41	0.19	0.31	0.53	0.07
MnO	*n.d.*	*n.d.*	0.01	*n.d.*	*n.d.*	0.03	0.00	0.08	0.00	0.05
MgO	0.30	0.28	0.34	0.23	0.23	0.26	0.33	0.70	0.38	0.30
CaO	55.0	54.4	54.0	54.9	55.7	54.4	54.9	55.2	55.1	54.8
SrO	1.48	1.27	1.49	1.37	1.26	1.23	1.27	0.53	0.69	1.40
BaO	0.10	*n.d.*	0.15	0.02	0.02	0.02	0.02	*n.d.*	0.10	0.06
Na_2O	0.05	0.01	0.04	*n.d.*	*n.d.*	0.03	0.02	0.10	0.09	0.01
CO_2	43.2	42.7	42.4	43.1	43.7	42.7	43.1	43.3	43.2	43.0
Total	100.15	98.81	98.47	99.85	101.21	99.14	99.82	100.25	100.09	99.70

Table 5a: New bulk rock geochemical data by XRF and ICP-MS (full data set in supplementary information)

Locality, region	Maniitsorssuaq, Sisimuit											
Rock classification	mela aillikite											
Sample no.	513567	513568	513573	513575	513588	513591	513595	517903	517905	517907	517908	517910
Major element analysis (wt %)												
SiO_2	30.90	34.50	33.40	32.60	33.90	32.80	30.70	33.30	34.00	32.10	34.30	32.70
TiO_2	3.75	4.79	4.78	4.29	4.90	3.52	3.67	4.61	4.54	3.56	4.81	4.58
Al_2O_3	2.39	4.34	3.90	2.59	3.62	2.43	2.37	3.78	4.34	2.81	3.79	2.18
FeO_T	12.68	13.80	13.66	13.44	14.09	11.96	12.12	13.69	13.72	12.39	14.12	14.22
MnO	0.19	0.20	0.20	0.20	0.21	0.21	0.19	0.21	0.21	0.21	0.22	0.20
MgO	26.10	22.30	23.40	27.60	25.00	28.90	26.20	22.80	21.20	25.80	24.10	27.70
CaO	8.26	11.09	9.90	8.15	9.54	7.79	7.55	10.61	11.58	10.61	9.84	8.50
Na_2O	0.21	0.22	0.32	0.12	0.18	0.24	0.28	0.32	0.28	0.20	0.19	0.15
K_2O	1.39	2.54	2.18	1.63	2.18	1.80	1.31	2.29	2.55	1.78	2.20	1.56
P_2O_5	0.43	0.40	0.37	0.35	0.41	0.21	0.36	0.50	0.56	0.64	0.41	0.43
H_2O	8.90	2.50	3.80	3.80	2.10	6.20	11.10	4.00	3.00	5.50	1.90	3.30
CO_2	2.30	0.80	1.50	2.60	1.20	1.40	1.70	1.30	1.50	1.80	1.50	1.70
Oxide sum	97.48	97.48	97.43	97.35	97.33	97.39	97.52	97.44	97.52	97.41	97.39	97.23
LOI	11.20	3.30	5.30	6.40	3.30	7.60	12.80	5.30	4.50	7.30	3.40	5.00
Fe_2O_3	-	-	-	-	-	-	-	-	-	-	-	-
FeO	-	-	-	-	-	-	-	-	-	-	-	-
Bulk rock parametres												
Phlogopite (wt.%)*	3.1	5.6	4.8	3.6	4.8	4.0	2.9	5.1	5.6	3.9	4.9	3.5
Ba in phlogopite (µg/g)*	179	139	153	170	151	167	187	155	149	171	154	143
Serpentine (wt.%)**	67.9	17.6	27.8	28.2	14.5	46.7	84.3	29.1	21.3	41.0	12.8	24.5
Max MgO lost (wt.%)***	9.9	2.6	4.0	4.1	2.1	6.8	12.3	4.2	3.1	6.0	1.9	3.6
Max SiO_2 added (wt.%)***	4.9	1.3	2.0	2.0	1.0	3.4	6.1	2.1	1.5	3.0	0.9	1.8
H_2O in Serpentine (wt.%)***	8.8	2.3	3.6	3.7	1.9	6.1	10.9	3.8	2.8	5.3	1.7	3.2
Trace element data (µg/g)												
Sc	13.7	25.4	18.6	15.7	21.5	16.6	13.7	21.5	21.5	16.6	20.6	13.7
V	184	228	214	180	219	167	162	221	253	198	208	200
Cr	1242	1050	1223	1428	1281	1626	1383	1127	999	1402	1217	1421
Co	106	98	107	112	106	108	105	100	102	102	110	120
Ni	887	705	784	969	845	1060	858	746	674	924	850	1029
Rb	54.0	94.6	79.2	61.3	85.2	61.8	52.6	81.8	92.1	67.0	81.5	50.3
Sr	831	731	752	868	733	884	758	828	855	1110	635	933

Table 5a cont..: New bulk rock geochemical data by XRF and ICP-MS (full data set in supplementary information)

Locality, region	Maniitsorssuaq, Sisimuit											
Rock classification	mela aillikite											
Sample no.	513567	513568	513573	513575	513588	513591	513595	517903	517905	517907	517908	517910
Trace element data (µg/g) cont..												
Y	11.1	10.7	11.7	11.2	12.0	11.0	10.0	12.0	11.3	12.6	12.5	11.8
Zr	222.6	330.3	360.6	239.8	324.9	196.5	205.5	353.2	408.7	286.9	343.3	215.1
Nb	126.1	131.4	135.6	136.9	160.7	135.7	125.0	137.5	133.0	149.3	147.4	140.3
Ba	527.6	749.7	705.7	586.0	697.1	638.7	519.9	753.6	807.2	647.3	720.0	472.1
La	86.4	76.5	89.0	100.0	96.0	98.9	89.0	83.0	76.7	94.0	93.0	100.2
Ce	174.1	153.3	180.1	204.4	193.9	205.1	186.2	168.2	149.9	186.6	185.4	202.1
Pr	19.9	17.8	20.9	23.9	22.1	23.9	21.3	18.7	16.7	21.5	20.6	23.4
Nd	73.9	64.9	75.5	86.0	79.3	87.0	78.2	71.7	58.8	78.5	72.9	86.2
Sm	9.5	8.6	10.1	11.1	10.6	11.1	9.9	9.0	8.3	10.4	9.7	11.6
Eu	2.6	2.3	2.7	3.0	2.9	3.0	2.6	2.5	2.2	2.7	2.7	3.0
Gd	6.9	6.3	6.9	7.9	7.4	7.5	6.8	6.5	6.0	7.0	6.8	7.8
Tb	0.74	0.68	0.79	0.85	0.87	0.82	0.72	0.75	0.72	0.79	0.83	0.84
Dy	3.44	3.49	3.96	3.57	3.93	3.97	3.12	3.52	3.42	3.52	3.71	3.42
Ho	0.44	0.49	0.49	0.53	0.52	0.49	0.41	0.52	0.51	0.54	0.49	0.54
Er	1.02	0.94	1.05	1.01	1.13	1.04	0.99	0.99	1.21	1.20	1.09	0.94
Tm	0.13	0.13	0.14	0.13	0.16	0.13	0.12	0.16	0.14	0.14	0.14	0.13
Yb	0.60	0.68	0.73	0.67	0.70	0.67	0.61	0.82	0.82	0.83	0.74	0.65
Lu	0.07	0.08	0.09	0.08	0.08	0.08	0.08	0.09	0.09	0.09	0.09	0.08
Hf	5.51	9.88	9.07	6.56	8.91	4.70	5.59	8.83	10.36	6.64	8.91	5.10
Ta	10.45	10.72	12.35	12.71	13.07	12.71	11.63	11.00	9.55	10.63	11.09	13.16
Th	7.19	6.89	8.86	10.05	8.77	9.55	9.65	7.68	6.99	8.08	8.96	9.55
U	3.59	3.00	3.78	3.68	4.07	4.07	2.23	3.30	3.10	3.78	3.59	4.26

* Phlogopite (wt.%) is calculated by mass balance assuming that all K_2O is in stoichiometric phlogopite. Ba in phlogopite is estimated by mass balance Assuming that all Ba is in phlogopite. Although phlogopite is the major Ba containing phase, barite is observed as an accessory phase in the groundmass hence the wt.% phlogopite represents a maximum estimate.

** Serpentine (wt%) is calculated by mass balance assuming that all remaining water is not included in phlogopite is present in stoichiometric serpentine. Due to the presence of clay minerals in kimberlite this calculation is a maximum estimate of the actual serpentine content.

*** The maximum MgO loss and SiO_2 due to serpentine alteration of olivine are calculated according to the reactions of Sparks *et al*. (2009). No account has been made for volume loss or gain of serpentine replacing carbonate. Since the calculated serpentine content is a maximum estimate these should be considered as maximum estimates of the effect of serpentine alteration.

Table 5b: New bulk rock geochemical data by XRF and ICP-MS

Locality, region	P-Dyke, Sarfartoq											Sarfartoq, Safartuup Nuna (S)			
Rock classification	transitional between calcite-kimberlite and ailikite											aillikte			
Sample no.	513501	513502	513503	513504	513505	513506	513507	513508	513509	513511	513512	513534	513535	513536	513537
Major element analysis (wt %)															
SiO_2	32.00	29.30	29.40	29.80	30.60	31.40	30.40	30.10	31.70	29.70	32.30	29.70	30.50	29.30	30.30
TiO_2	1.42	1.62	1.26	1.53	0.96	0.97	1.41	1.28	2.03	1.26	1.39	2.84	3.25	3.69	2.90
Al_2O_3	1.15	1.12	0.45	0.89	0.88	0.28	1.23	0.96	0.73	0.60	1.17	1.90	1.98	2.29	1.76
FeO_T	10.45	9.32	10.16	9.91	9.33	10.11	10.09	9.89	10.71	9.23	10.02	11.67	12.23	12.24	11.50
MnO	0.15	0.14	0.17	0.16	0.15	0.17	0.15	0.16	0.18	0.15	0.18	0.17	0.17	0.18	0.17
MgO	32.40	32.40	35.00	34.60	34.80	33.80	33.80	32.50	35.80	35.20	34.80	27.00	27.70	25.20	28.20
CaO	3.88	6.35	5.27	5.74	5.11	4.14	4.91	6.05	4.58	4.76	6.47	9.20	9.29	10.63	7.76
Na_2O	0.08	0.10	0.09	0.07	0.07	0.07	0.05	0.08	0.04	0.04	0.05	0.12	0.30	0.31	0.10
K_2O	0.52	0.44	0.15	0.40	0.40	0.14	0.58	0.50	0.35	0.24	0.84	0.86	1.02	1.28	0.75
P_2O_5	0.16	0.18	0.22	0.20	0.09	0.17	0.23	0.19	0.15	0.21	0.23	0.34	0.37	0.48	0.37
H_2O	10.50	7.50	10.80	9.70	10.30	11.00	10.70	8.50	6.10	11.30	4.80	7.90	3.00	3.20	6.80
CO_2	4.90	8.90	4.50	4.40	4.30	5.40	3.90	7.40	5.10	4.70	5.30	5.80	7.30	8.30	6.20
Oxide sum	99.26	98.43	98.53	98.54	98.07	99.28	98.52	99.26	99.21	98.37	99.15	98.86	98.39	98.45	98.01
LOI	15.40	16.44	15.27	14.07	14.63	16.40	14.58	15.90	11.20	15.96	10.10	13.75	10.28	11.52	12.95
Fe_2O_3	-	6.32	7.66	7.35	6.63	-	7.86	-	-	6.99	-	7.22	4.57	3.63	5.99
FeO	-	3.63	3.27	3.30	3.37	-	3.02	-	-	2.94	-	5.17	8.12	8.98	6.11
Bulk rock parametres.															
Phlogopite (wt.%)*	1.2	1.0	0.3	0.9	0.9	0.3	1.3	1.1	0.8	0.5	1.9	1.9	2.3	2.8	1.7
Ba in phlogopite (µg/g)*	389	184	605	297	393	835	541	444	165	210	331	170	144	145	180
Serpentine (wt.%)**	80.6	57.6	82.7	74.4	79.3	84.7	82.2	64.7	47.0	86.8	36.2	60.3	22.2	23.7	51.7
Max MgO lost (wt.%)***	11.7	8.4	12.0	10.8	11.5	12.3	12.0	9.4	6.8	12.6	5.3	8.8	3.2	3.4	7.5
Max SiO_2 added (wt.%)***	5.8	4.2	6.0	5.4	5.7	6.1	5.9	4.7	3.4	6.3	2.6	4.4	1.6	1.7	3.7
H_2O in serpentine (wt.%)***	10.5	7.5	10.7	9.7	10.3	11.0	10.7	8.4	6.1	11.3	4.7	7.8	2.9	3.1	6.7
Trace element data (µg/g)															
Sc	9.8	9.0	7.9	8.0	7.8	6.9	9.2	9.8	8.8	7.0	9.8	13.6	14.0	16.5	13.5
V	76	67	81	85	42	60	102	82	65	63	96	138	161	201	162
Cr	1842	1531	1406	1424	1363	1987	1540	1817	2025	1697	1678	1375	1542	1728	1564
Co	104	95	102	103	92	104	97	100	103	100	100	98	100	94	106
Ni	1266	1333	1424	1403	1388	1407	1361	1303	1364	1494	1334	986	984	852	1084
Rb	23.5	10.4	6.0	14.3	16.5	4.2	27.8	21.0	8.5	6.4	30.7	43.3	55.8	66.2	38.1
Sr	299	406	588	472	230	365	552	406	363	462	552	620	631	786	543

Table 5b cont..: New bulk rock geochemical data by XRF and ICP-MS (full data set in supplementary information)

Locality, region	P-Dyke, Sarfartoq											Sarfartoq, Safartuup Nuna (S)			
Rock classification	transitional between calcite-kimberlite and ailikite											aillikte			
Sample no.	513501	513502	513503	513504	513505	513506	513507	513508	513509	513511	513512	513534	513535	513536	513537
Trace element data (µg/g) cont..															
Y	5.5	5.7	5.6	7.2	6.6	5.5	5.8	6.9	6.6	5.6	7.7	8.6	10.0	11.8	9.5
Zr	55.4	52.7	82.2	56.3	33.1	37.0	98.6	58.4	46.6	34.1	57.0	176.4	213.1	273.1	211.4
Nb	87.2	105.2	87.7	108.2	56.7	53.6	95.2	73.2	119.8	86.1	89.4	90.2	97.9	114.6	90.2
Ba	442.3	176.8	191.5	256.2	340.1	255.7	673.8	485.7	126.4	107.2	608.2	317.5	318.3	404.1	291.1
La	71.2	83.9	76.0	89.7	60.8	57.6	73.4	62.0	101.7	76.2	76.6	50.3	55.4	64.5	51.1
Ce	152.4	171.9	164.7	183.6	107.7	122.6	154.7	128.3	204.8	163.7	151.6	112.9	125.8	144.0	114.4
Pr	17.1	19.3	18.7	20.2	11.3	14.2	17.6	14.4	23.0	18.5	17.2	13.9	15.3	17.5	14.2
Nd	61.2	67.7	66.5	71.4	43.0	52.2	62.3	53.4	82.2	65.4	61.0	54.3	59.7	68.2	56.0
Sm	7.6	8.4	8.1	9.1	5.3	6.3	7.5	6.4	10.2	8.0	7.6	8.3	9.1	10.4	8.5
Eu	1.8	2.0	2.0	2.2	1.3	1.5	1.8	1.6	2.5	1.9	1.9	2.2	2.5	2.8	2.3
Gd	4.3	5.3	5.2	6.0	4.0	3.7	4.8	4.0	6.4	5.1	4.7	5.8	6.3	7.3	6.0
Tb	0.43	0.58	0.54	0.65	0.46	0.39	0.54	0.41	0.62	0.56	0.52	0.66	0.71	0.83	0.67
Dy	1.65	2.27	2.12	2.55	1.90	1.65	2.12	1.78	2.37	2.13	2.16	2.70	3.07	3.51	2.91
Ho	0.23	0.25	0.24	0.31	0.25	0.20	0.25	0.25	0.28	0.23	0.29	0.38	0.42	0.48	0.39
Er	0.48	0.68	0.67	0.78	0.76	0.52	0.66	0.64	0.63	0.66	0.77	0.86	0.98	1.15	0.95
Tm	0.05	0.06	0.06	0.07	0.06	0.06	0.05	0.07	0.07	0.05	0.08	0.08	0.10	0.12	0.10
Yb	0.27	0.30	0.32	0.37	0.37	0.31	0.30	0.37	0.34	0.31	0.50	0.45	0.52	0.65	0.53
Lu	0.03	0.03	0.03	0.04	0.05	0.04	0.04	0.05	0.03	0.04	0.07	0.05	0.06	0.08	0.06
Hf	1.59	1.99	1.90	1.73	1.12	1.14	2.31	1.50	1.41	1.06	1.76	4.38	5.12	6.41	5.04
Ta	7.40	8.93	8.18	8.60	5.17	6.53	7.87	6.24	10.09	8.54	7.30	8.31	8.96	10.09	8.11
Th	9.85	9.84	10.70	9.80	6.79	9.65	9.09	8.68	11.31	9.73	9.17	4.74	5.12	5.90	4.78
U	1.92	2.03	1.78	2.10	1.09	1.41	1.74	1.51	2.42	1.50	1.92	1.39	1.29	1.48	1.19

* Phlogopite (wt.%) is calculated by mass balance assuming that all K_2O is in stoichiometric phlogopite. Ba in phlogopite is estimated by mass balance Assuming that all Ba is in phlogopite. Although phlogopite is the major Ba containing phase, barite is observed as an accessory phase in the groundmass hence the wt.% phlogopite represents a maximum estimate.

** Serpentine (wt%) is calculated by mass balance assuming that all remaining water is not included in phlogopite is present in stoichiometric serpentine. Due to the presence of clay minerals in kimberlite this calculation is a maximum estimate of the actual serpentine content.

*** The maximum MgO loss and SiO_2 due to serpentine alteration of olivine are calculated according to the reactions of Sparks *et al*. (2009). No account has been made for volume loss or gain of serpentine replacing carbonate. Since the calculated serpentine content is a maximum estimate these should be considered as maximum estimates of the effect of serpentine alteration.

Table 6: Mixing models*

				mass fraction end-members						
	PKM	**LM**	**HARZ**	**SiO_2**	**Al_2O_3**	**FeO_T**	**MgO**	**CaO**	**K_2O**	**CO_2**
HARZ (depleted peridotite xenoliths)				35.4	1.0	12.7	43.9	0.3	0.0	0.0
LM (melt derived from glimmerite)				39.5	13.3	20.4	8.5	6.3	6.5	0.0
PKM (primary kimberlite melt)				17.3	1.8	8.1	23.9	19.5	0.4	18.8
Majuagaa - bulk average data				25.6	1.4	10.2	33.1	10.6	0.2	10.1
Majuagaa - mixing model	0.55	0	0.45	25.4	1.4	10.2	32.9	10.9	0.2	10.3
Majuagaa - melt estimate				17.7	1.7	8.2	24.3	19.1	0.4	18.4
P-Dyke - bulk average data				30.6	0.9	9.9	34.1	5.2	0.4	5.3
P-Dyke - mixing model	0.38	0.03	0.6	28.7	1.6	11.2	35.5	7.7	0.3	7.1
P-Dyke - melt estimate				23.4	0.6	5.7	19.5	12.6	1.0	13.3
Sarfartuup Nuna (S) - bulk average				30.5	1.9	12.1	28.1	9.0	0.9	6.5
Sarfartuup Nuna (S) - mixing model	0.38	0.25	0.38	29.6	4.4	12.9	27.5	9.0	1.8	7.1
Sarfartuup Nuna (S) - melt estimate				27.5	2.4	11.7	18.6	14.2	1.4	10.4
Maniitsorsuaq - bulk average data				33.0	3.2	13.3	25.1	9.5	2.0	1.6
Maniitsorsuaq - mixing model	0.3	0.35	0.35	31.4	5.6	14.0	25.5	8.2	2.4	5.6
Maniitsorsuaq - melt estimate				36.9	4.2	15.0	20.8	8.8	2.9	-3.0

* Estimation of the proportions of the contributions of three theoretical end-members to the bulk rock compositions: PKM – primary kimberlite melt (Pilbeam *et al*., 2023); HARZ – ilmenite-harzburgite average assimilate for Majuagaa (Pilbeam *et al.,* 2023); and LM – melt from phlogopite-clinopyroxene veins (Foley *et al*., 1999). The melt compositions proposed are calculated by projecting the average bulk rock analyses from HARZ onto the join between PKM and LM. We emphasize that these models should be considered order of magnitude estimates (as indicated by the fit of model to data shown in Fig. 17).

.

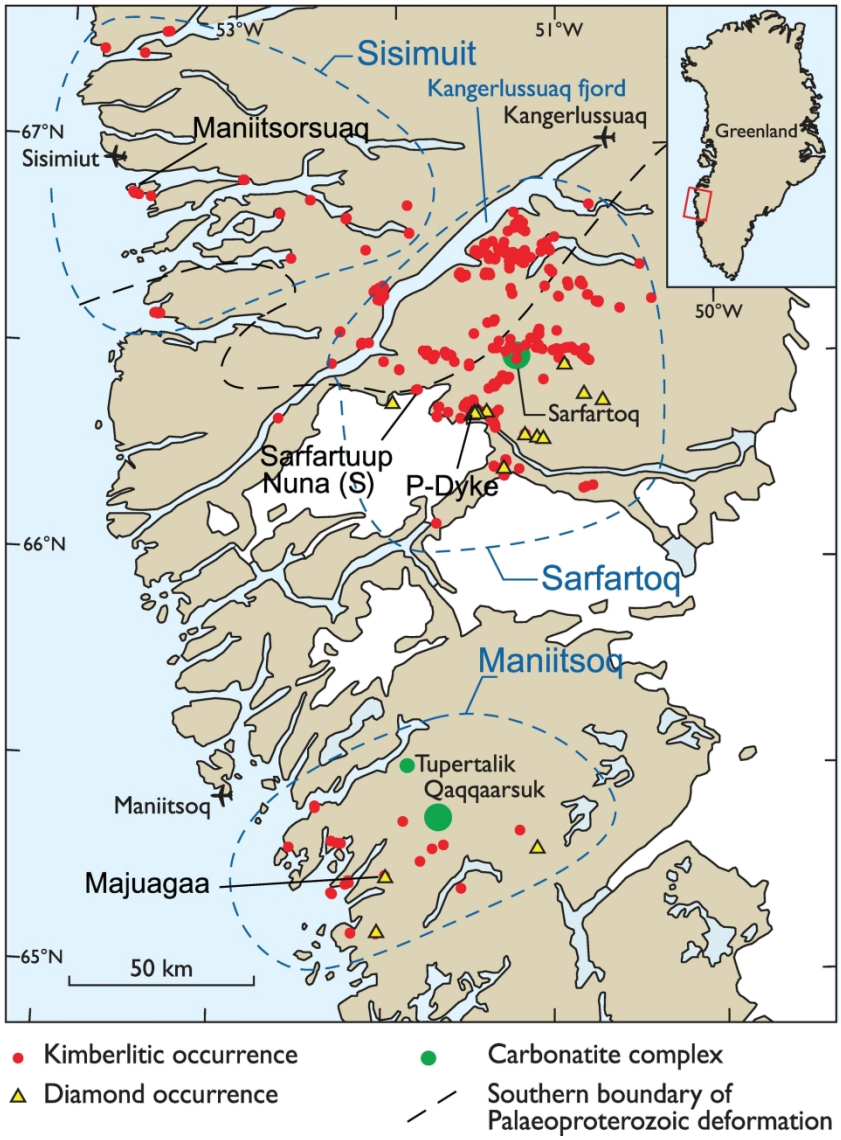

Fig. 1

166x237mm (300 x 300 DPI)

Fig. 2: Field photographs

170x124mm (600 x 600 DPI)

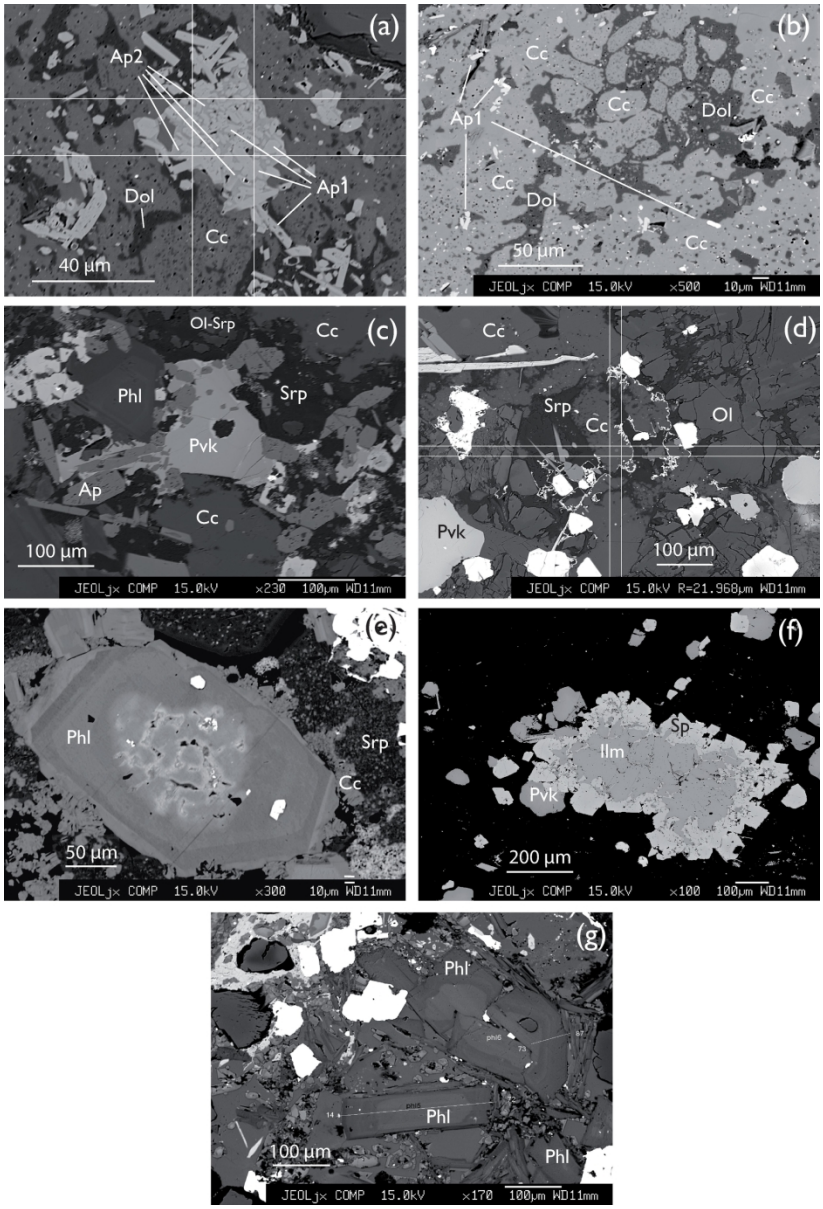

Fig. 3

172x253mm (300 x 300 DPI)

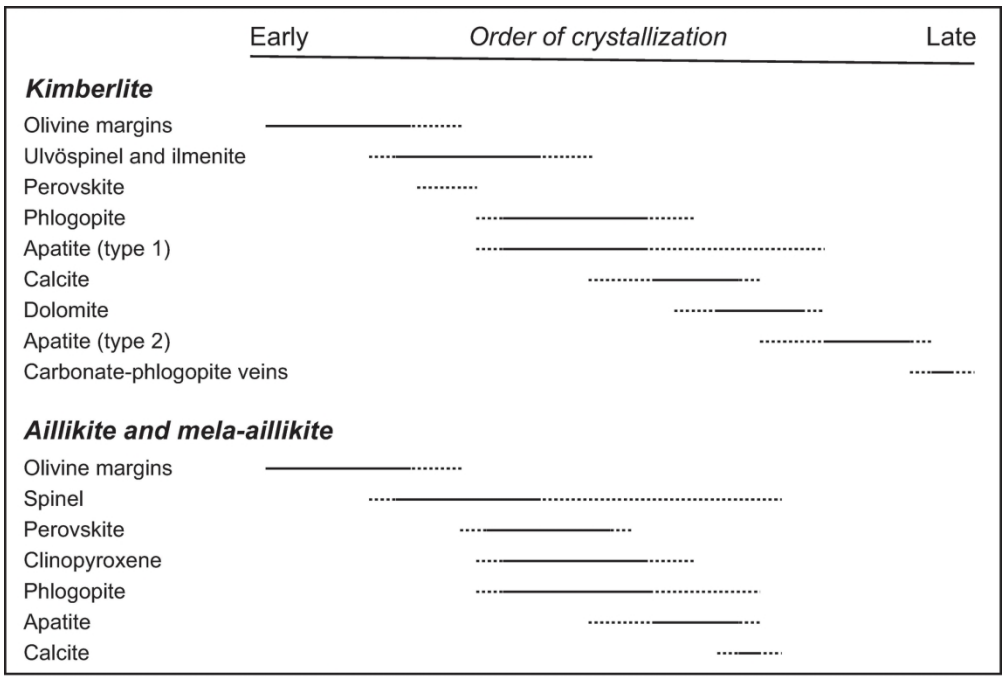

Fig. 4

162x135mm (300 x 300 DPI)

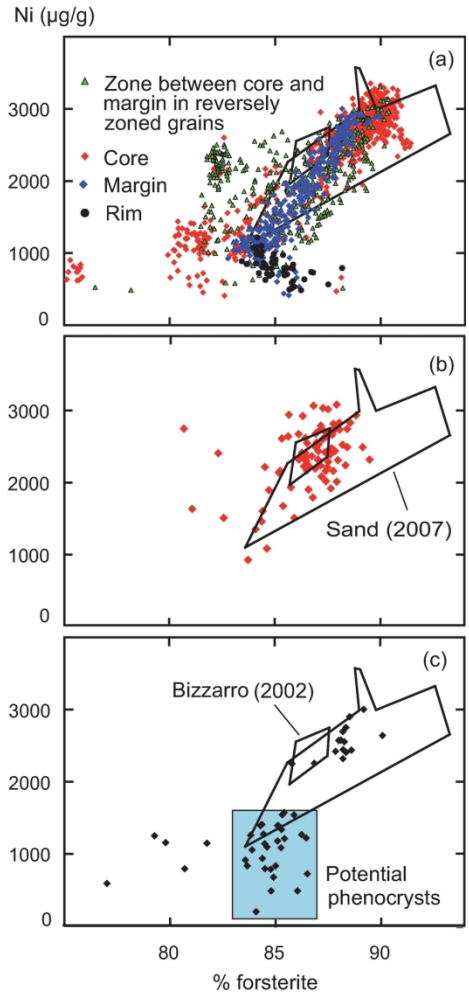

Fig. 5

110x202mm (300 x 300 DPI)

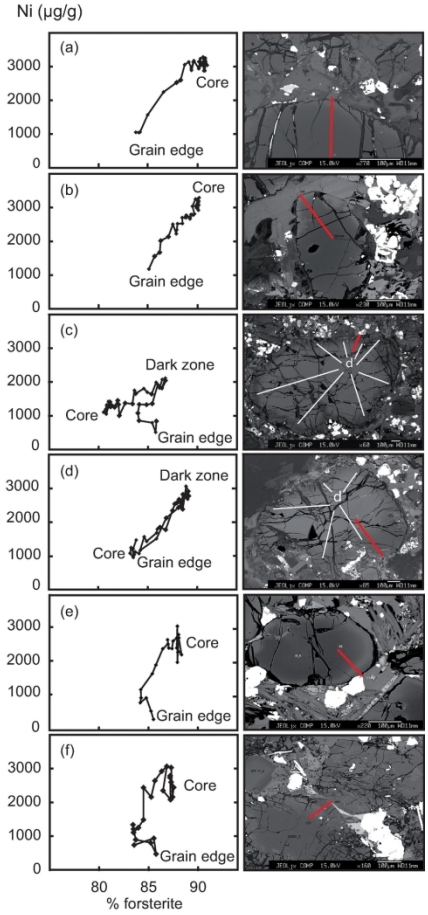

Fig. 6

105x223mm (300 x 300 DPI)

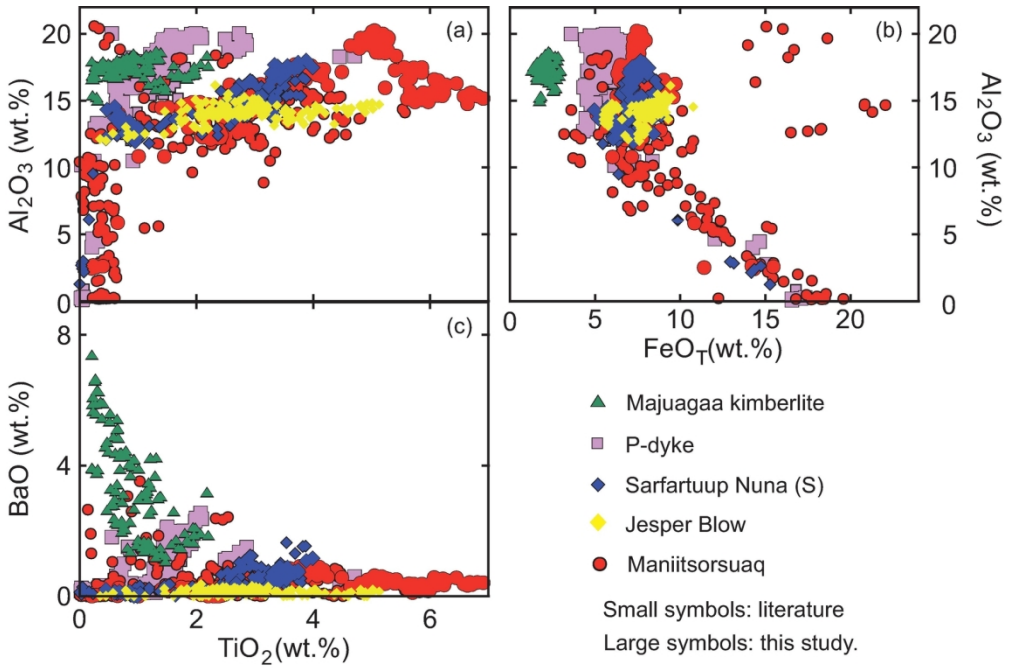

Fig. 7

158x105mm (300 x 300 DPI)

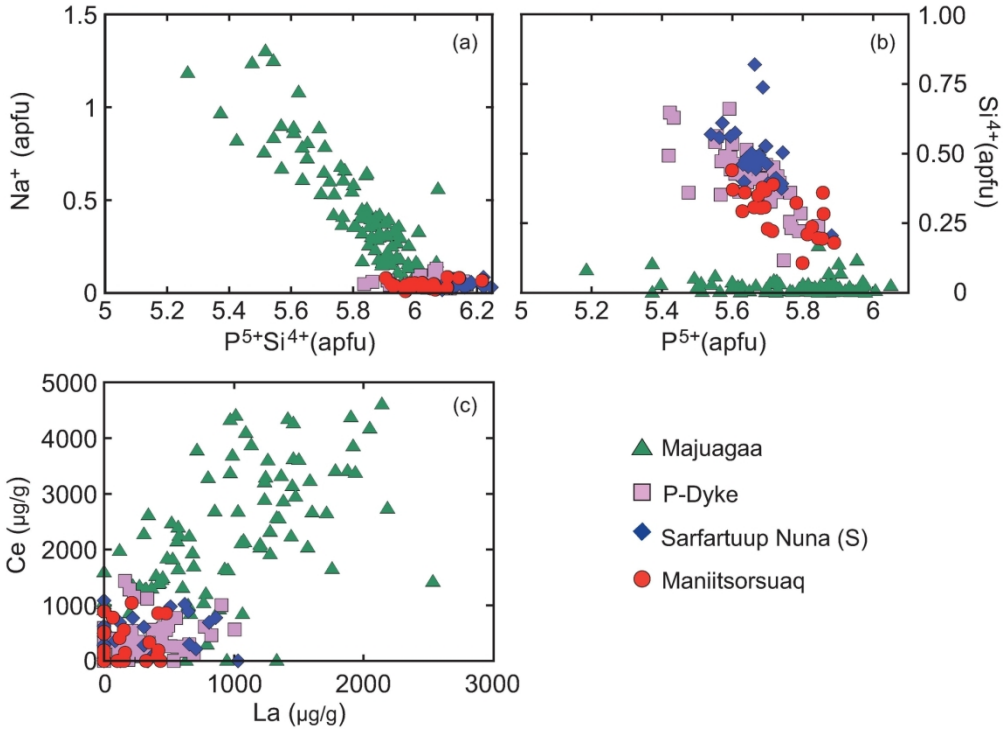

Fig. 8

167x121mm (300 x 300 DPI)

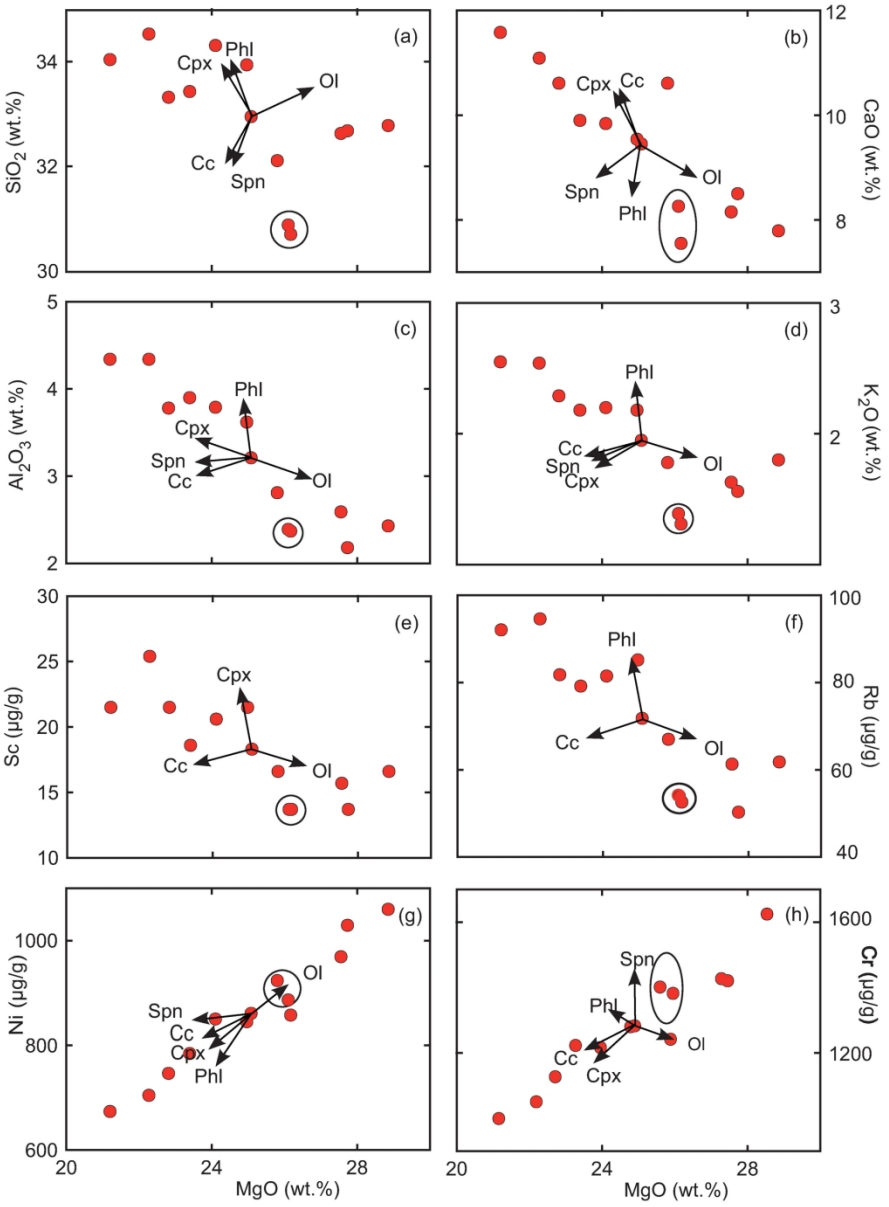

Fig. 9

168x214mm (300 x 300 DPI)

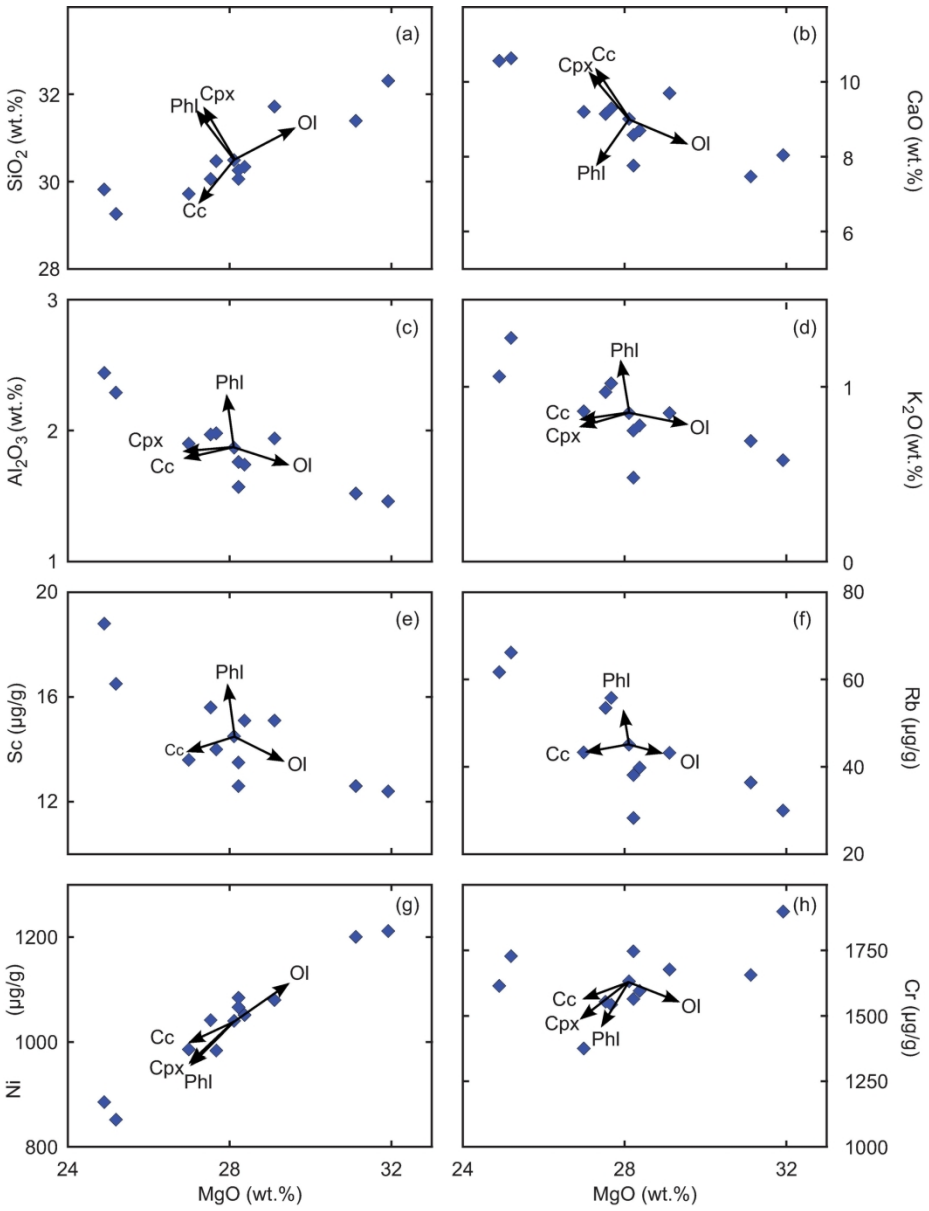

Fig. 10

164x214mm (300 x 300 DPI)

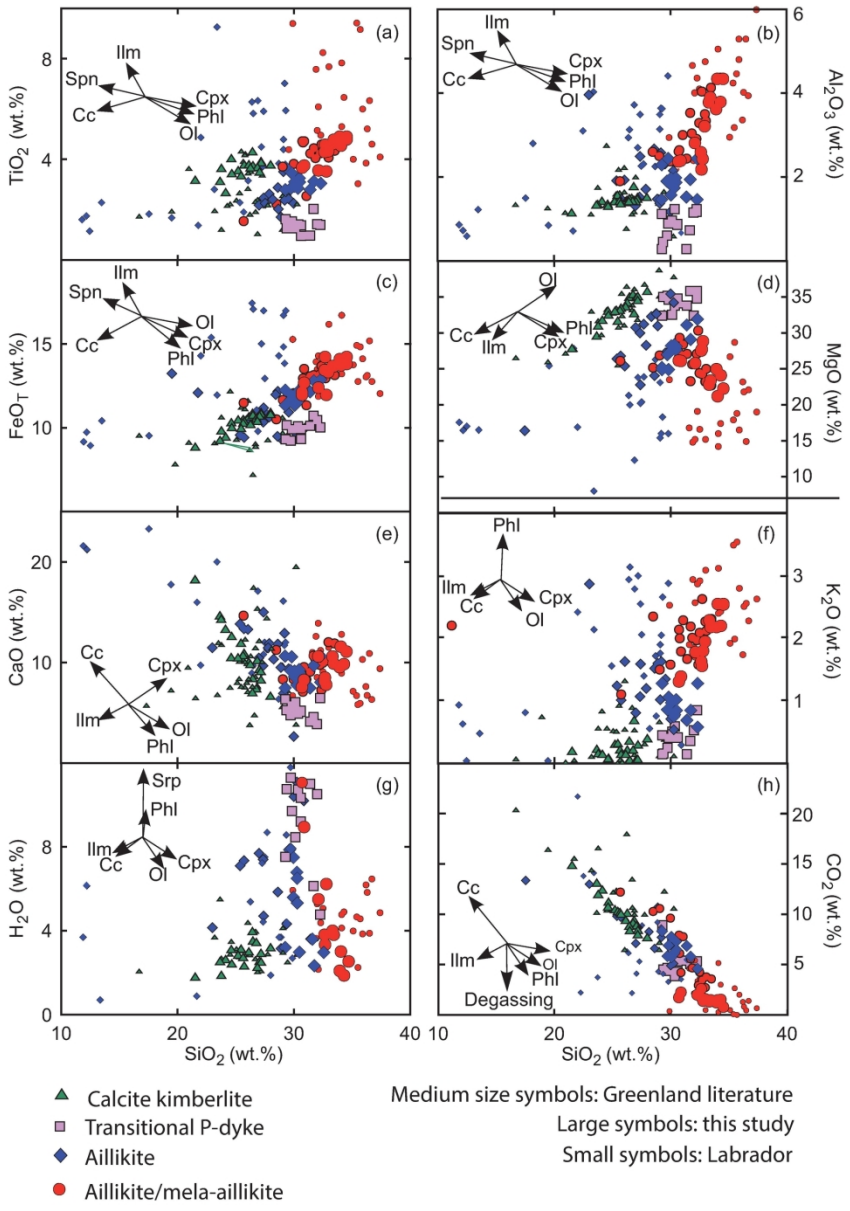

Fig. 11

169x222mm (300 x 300 DPI)

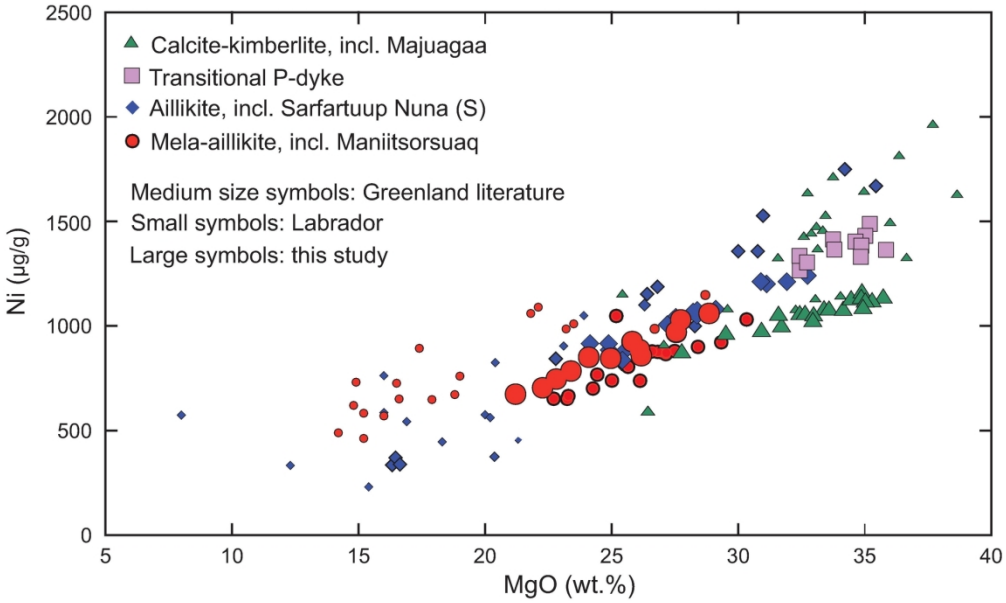

Fig. 12

169x101mm (300 x 300 DPI)

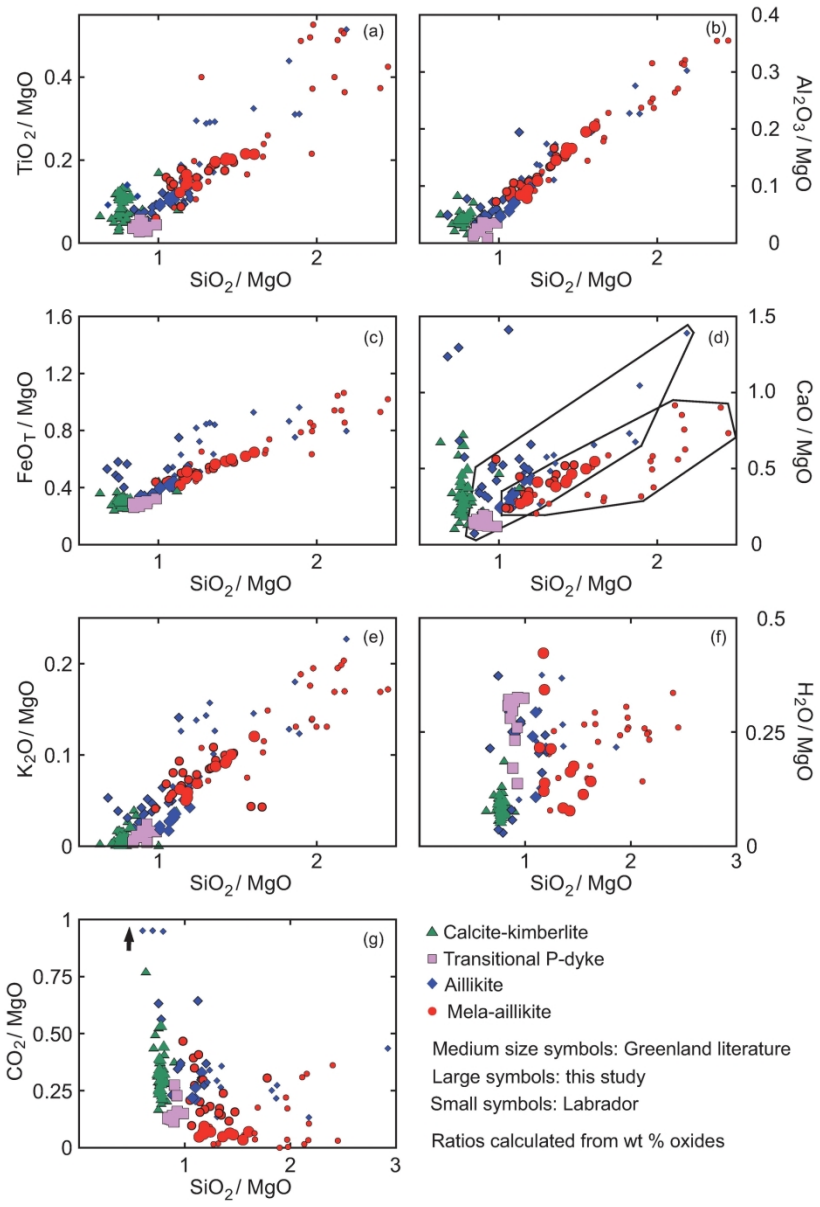

Fig. 13

166x245mm (300 x 300 DPI)

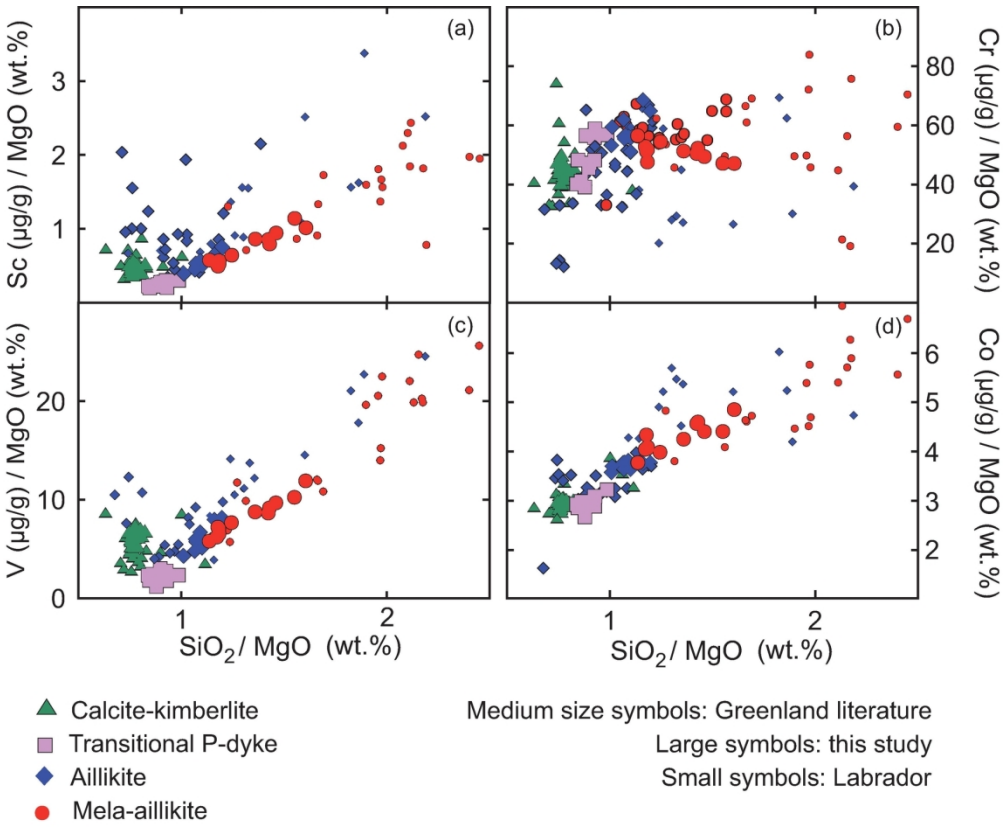

Fig. 14

157x129mm (300 x 300 DPI)

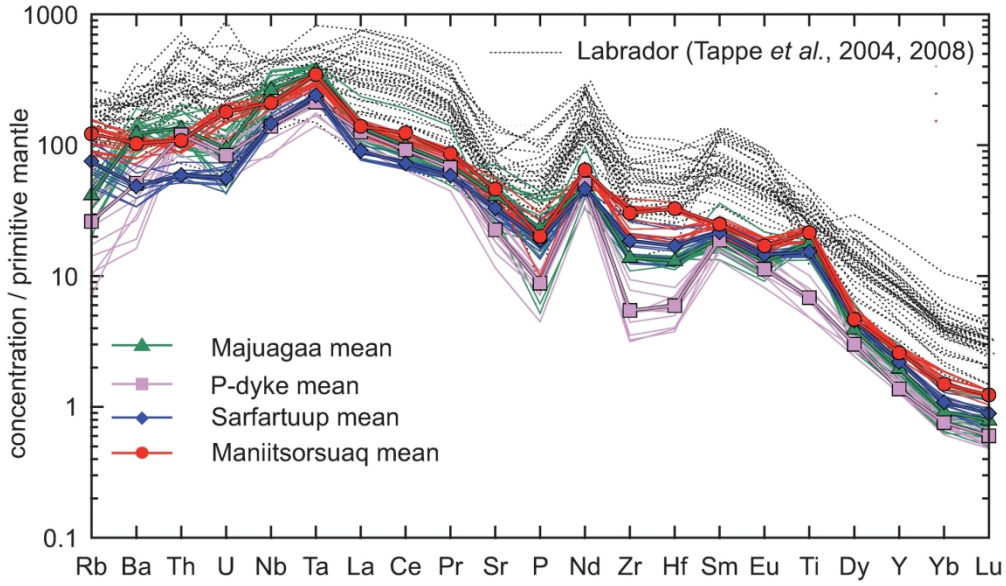

Fig. 15

166x96mm (300 x 300 DPI)

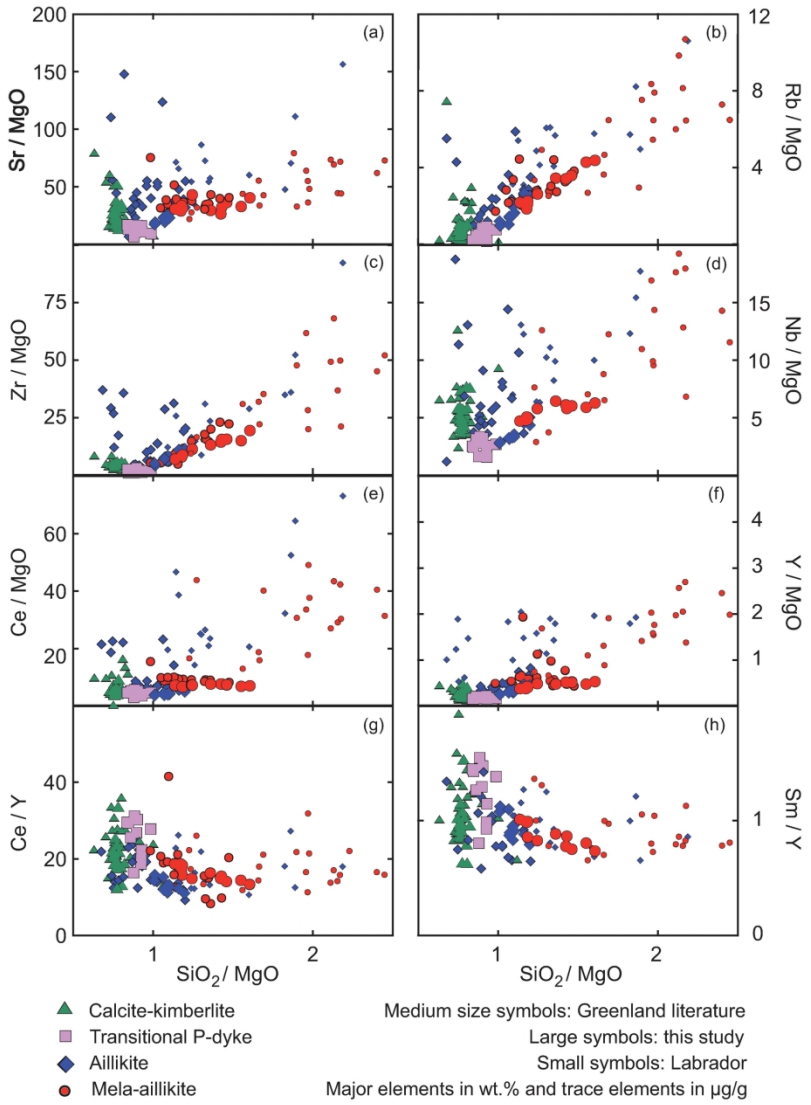

Fig. 16

162x243mm (300 x 300 DPI)

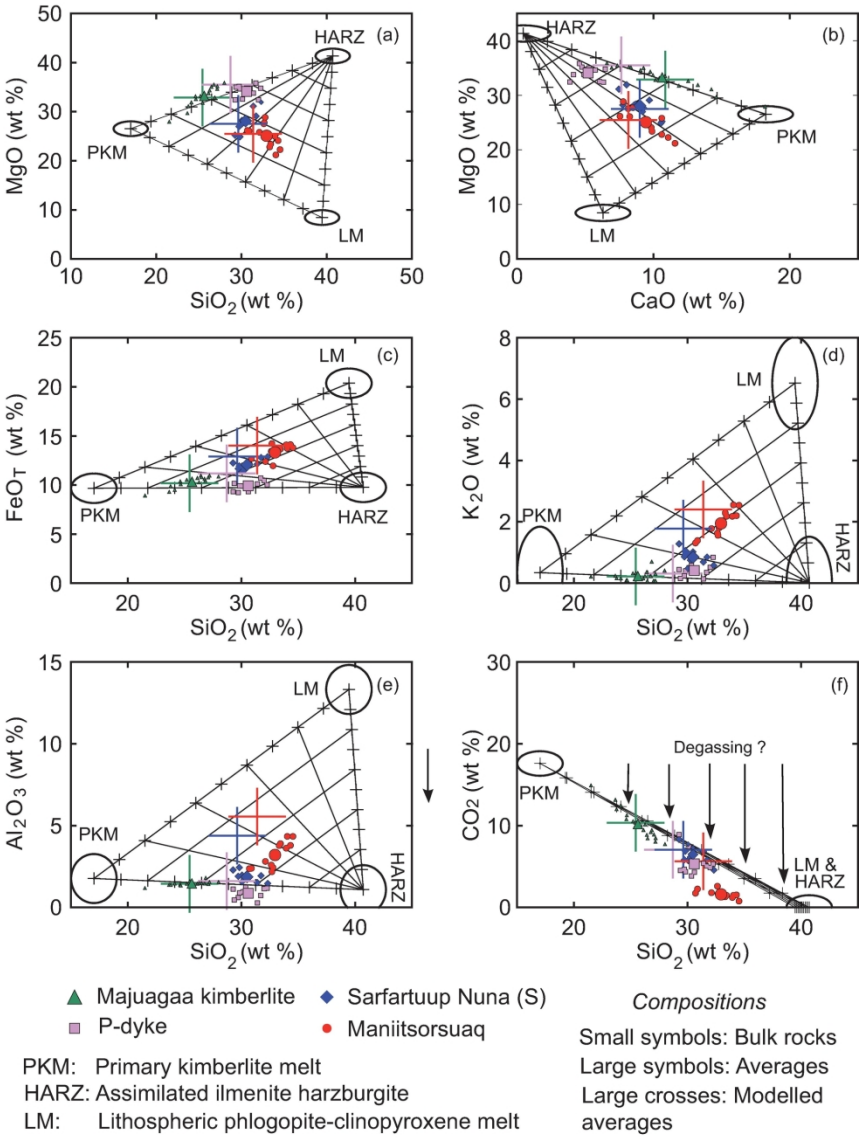

Fig. 17

162x228mm (300 x 300 DPI)